Principal Investigator/Project Director: Brian G. Thomas

Institution: University of Illinois at Urbana-Champaign

Award Number: DMI- 01-15486

Program: Materials Processing & Manufacturing

Project Title:

Flow Dynamics and Inclusion Transport in Continuous Casting of Steel

B.G. Thomas, W. Grafton & Lillian B. Wilkins Professor

Q. Yuan, PhD Student

L. Zhang, Research Associate

Bin Zhao, MS Student

S.P. Vanka, Professor

University of Illinois at Urbana-Champaign
Department of Mechanical and Industrial Engineering
1206 West Green Street, Urbana, IL 61801
Ph: 217-333-6919, 217-244-4656; Fax: 217-244-6534;
Email: bgthomas@uiuc.edu

ABSTRACT

The quality of continuous cast steel depends greatly on the extent of inclusion particle entrapment, which is governed by flow transport phenomena in the mold region. As part of a long-term effort to develop and apply comprehensive models of these and other phenomena, this paper reports on work during the second year of this NSF grant that aims 1) to develop quantitative models of transient flow of molten steel, superheat and inclusions during the continuous casting of steel, and 2) to apply them to improve understanding and efficiency of inclusion particle removal in the process.

Results are reported here for five interrelated subprojects. Firstly, models of transient flow using Large Eddy Simulation (LES), which were previously validated and used to predict flow, are used here to predict the accompanying transport of inclusion particles. Of most significance, the model can predict the ultimate distribution of inclusions in the final product. Models are then applied to investigate the effect of nozzle geometry on flow and inclusion removal. Thirdly, model improvements are presented to predict inclusion size distribution evolution. As inclusion removal in the mold is shown to be quite small, simulations are extending upstream to investigate inclusion removal during ladle refining. Fourthly, behavior of the top surface flux layers, which is important to inclusion removal, is computed, including the effects of natural convection. Finally, accurate simulation of superheat transport in the molten pool due to jet impingement is demonstrated.

1. INTRODUCTION

There are great economic, environmental and safety incentives for understanding how to lower the inclusion content of steel. Lowering inclusion-related defects improves steel minimum strength, fatigue life, surface appearance, yield and energy efficiency (from reduced rejects), and thereby increase steel industry competitiveness. Consistent lower inclusions levels would allow thinner gage products (with associated weight and energy savings) and could reduce the need for costly and energy-intensive secondary refining steps, such as vacuum arc refining and electroslag remelting. Continuous casting produces 96% of the steel manufactured in the U.S. [1] and is the last, and most important, processing step where inclusions can either be generated or removed. This project investigates inclusion removal during this process through the use of computational models, validated with plant experiments.

Plant observations have found that many serious quality problems, including inclusion entrapment, are directly associated with the flow pattern in the mold.[2] Defects caused by nonoptimal fluid flow are even more important to the nearer-net-shape thin-slab casting processes, which are starting to transform the industry.[3] This is because higher velocities are required through a smaller inlet nozzle to cast a thin section slab with the same throughput. Thus, design and control of the fluid flow pattern in the continuous casting mold to minimize inclusions is of crucial importance to the steel industry.

The flow pattern in the mold can be controlled by many variables, including the nozzle and mold geometry, submergence depth, steel flow rate, argon injection rate, electromagnetic stirring, and flux layer properties. Many of these parameters are easy and inexpensive to change and yet have a profound influence on flow and corresponding quality. Currently, flow pattern design is done through trial and error, based on qualitative experiments with water models, plant trials, and the plant operator's experience with defects. Identifying an optimal flow pattern is very difficult, because the fundamental relationship between flow pattern and inclusion entrapment has not been quantified. Thus, each casting operation requires its own expensive experiments, and old defects often reappear when changes in the process occur. With so many different operations and new processes to optimize, the industry can no longer afford this approach.

In previous studies, the principal investigators have applied computational models to increase understanding of flow in the continuous casting mold, using both steady-state[4-21] and transient simulations.[22-29] The reliability of these models to predict flow has been demonstrated through comparison with both water models[9-11, 16, 19, 20, 24, 27, 28] and flow measurements in an operating steel

caster.[26, 28] The next step is to apply these models to investigate fundamentally, the associated transport and entrapment of inclusion particles and to determine quantitative relationships between flow pattern control parameters (eg. nozzle geometry) and particle entrapment. The current research is concerned with developing and applying such computations, combined with physical water modeling studies to validate the models and to provide further insight. Finally, plant trials are conducted to further validate the models, and to test proposed improvements. The results of this study should benefit to the steel industry by leading to increased fundamental understanding of inclusion entrapment, and to improvements in design and operating conditions that improve flow pattern in the continuous casting strand and lower costly defects.

2. THE PROCESS

A schematic of part of the continuous casting process is depicted in **Fig. 1**.[30] Steel from the ladle flows through the "tundish," and then it exits down through a ceramic Submerged Entry Nozzle (SEN) and into the mold. Here, the steel freezes against the water-cooled copper walls to form a thin solid shell, which is continuously withdrawn from the bottom of the mold at a "casting speed" that matches the flow of the incoming metal. Flow through the SEN is gravity driven by the pressure difference between the liquid levels of the tundish and the mold top free surfaces. The flow rate is controlled (using feedback from a level sensor) to maintain the liquid level in the mold as constant as possible. In one method, a "stopper rod" extends down through the tundish to partially plug the exit. In another method, a "slide gate" blocks off a portion of the SEN pipe section by moving a disk-shaped plate through a horizontal slit across the entire SEN. Such flow adjustment methods allow for independent control of casting speed and metal level, and are essential for stopping the flow of molten steel if the operation must be abruptly terminated. The submerged nozzle protects the molten steel from exposure to air, which helps to avoid reoxidation and inclusion formation. Together with the casting speed, mold geometry, argon gas injection rate, and other parameters, the nozzle geometry also controls the flow pattern created in the mold cavity. This flow pattern in turn controls the entrapment of inclusions and other defects which determine the steel quality.

3. THE PROBLEM

As shown in Fig. 1, jets of molten steel exit the nozzle and traverse across the mold cavity to impinge on the solidifying steel shell near the narrow faces. These jets carry bubbles and inclusion particles into the mold cavity. In addition, high speed flow across the top surface may shear droplets of

liquid mold slag into the flow, where they may become entrained in the liquid steel.[31] If the flow pattern enables the particles to reach the top surface, they should be harmlessly removed into the liquid slag layer. However, when the flow pattern is detrimental, particles become entrapped in the solidifying steel shell, where they cause serious quality problems and costly rejects. Particle trajectories and removal depend on particle size, which is further complicated by collisions and attachment to bubbles. Particles that become trapped near the meniscus generate surface delamination defects, and may initiate surface cracks. This is more likely when the meniscus partially freezes to form meniscus "hooks", which entrap particles into the solidifying meniscus before they can enter the liquid slag. Meniscus hooks are more prevalent there is insufficient liquid temperature at the meniscus. The local superheat of the molten steel near the meniscus depends on the flow pattern in the mold, as the jets also transport superheat. High velocities near the meniscus lead to excessive surface level fluctuations, which also enhances particle entrapment. This is also controlled by the flow pattern in the mold.

Particles which are entrained into the lower recirculation zones can gradually spiral and become trapped in the solidifying front deep inside the product,[15, 32] leading to internal cracks, slivers in the final rolled product, and blisters.[2] One of these defects, known as "pencil pipes"[31] is caused when small argon gas bubbles surrounded by inclusions are caught in the solidifying shell. During rolling, the inclusion clusters elongate to create long slivers in the final product. During subsequent annealing processes, the trapped bubbles expand to create surface blisters.[31] These intermittent defects are particularly costly because they are often not detected until after many subsequent finishing steps. Thus, there is a great incentive to understand how to control the mold flow pattern in order to minimize particle entrapment and the associated quality problems.

4. PREVIOUS RESULTS

In the first year of this project, significant advances were made on several aspects of this multifaceted research project involving dynamic flow and inclusion transport in the continuous casting mold. They are briefly summarized in last year's report [33]. These subprojects included: A) asymmetric transient flow in the mold, B) surface level, particle transport, and heat transfer in the molten pool; C) nucleation and growth of alumina inclusions in molten steel; D) effect of bubbles on inclusion removal; and E) inclusion removal in the steel caster.

5. CURRENT RESULTS

The results of this project are contained in 24 publications to date [33-56] and in our website **http://ccc.me.uiuc.edu**. This paper reports selected recent results on five different components of the current multifaceted research project:

1) Particle transport and entrapment in a continuous-cast thin slab

2) Parametric study: effect of nozzle geometry on inclusion entrapment

3) Nucleation and growth models for alumina inclusions in molten steel

4) Flow and heat transfer in a molten flux layer

5) Transient flow and superheat transport in continuous-cast steel slabs

5.1. Particle Transport and Entrapment in a Continuous-Cast Thin Slab

In this sub-project, Large-Eddy_Simulation models are developed to simulate the transient transport and entrapment of inclusion particles, using a Lagrangian approach based on previous computations of fluid flow in the continuous casting process [53]. Efforts focus on validation using measurements in both water models and analysis of actual steel samples. This present work investigates the transport and capture of small inclusions (10μm and 40μm) in a thin-slab steel caster, as described in detail elsewhere [54].

A. Model Description

The geometry and operating conditions of the thin-slab caster are given in Fig. 1 and Table I. Fluid flow and particle transport were computed in the model domain (Fig. 1) that includes the 1.11m submerged entry nozzle and the top 2.40m of a steel strand (*Case 2-S*). Three dimensional time-dependent turbulent fluid velocities were first obtained by solving the Navier-Stokes equations using large eddy simulations (LES) [53]. Special velocity boundary conditions [53] were applied to the fluid at the solidifying front in the steel caster to simulate the solidification effects. The transport of inclusion particles through this flow field was then modeled as follows.

(i) Governing Equations:

Particle transport was solved by integrating the following equations in a Lagrangian framework:

$$\mathbf{v}_p = \frac{d\mathbf{x}_p}{dt} \quad [1]$$

$$\frac{d\mathbf{v}_p}{dt} = \frac{18\rho\nu_0}{\rho_p d_p{}^2}\left(1+0.15\,\mathrm{Re}_p{}^{0.687}\right)\left(\mathbf{v}-\mathbf{v}_p\right)+(1-\frac{\rho}{\rho_p})\mathbf{g}+\frac{\mathbf{F}_{saff}}{m_p} \quad [2]$$

where:

$$\mathbf{g} = (0,\ 0,\ 9.81\mathrm{m/s}^2) \quad [3]$$

$$\mathrm{Re}_p = \frac{\left|\mathbf{v}-\mathbf{v}_p\right| d_p}{\nu_0} \quad [4]$$

$$\mathbf{F}_{saff} = 1.61 d_p^2 \left(\mu_0\rho\right)^{1/2} |\boldsymbol{\omega}|^{-1/2}\left[(\mathbf{v}-\mathbf{v}_p)\times\boldsymbol{\omega}\right] \quad [5]$$

and

$$\boldsymbol{\omega} = \nabla\times\mathbf{v} \quad [6]$$

The three terms on the RHS of Eq. [2] are due to the forces of drag (for Re_p<800), buoyancy (due to density difference) and Saffman lift (due to shear velocity gradients) for spherical particles. Re_p is the Reynolds number for creeping flow, based on the small difference between the fluid and particle velocities.

(ii) Initial and Boundary Conditions

Inclusions were introduced into the computational domain at the local fluid velocity. Their initial positions were chosen randomly in the edges of a cylindrical region in the tundish above the submerged entry nozzle. The results of the separate simulation of fluid flow and particle trajectories in the nozzle itself were used to determine the particle locations in the nozzle outlet port planes for the strand simulation. Inclusions touching the top surface were assumed to be removed.

(iii) Modeling of Particle Capture by the Solidification Front

In a steel caster, inclusions may be trapped when they touch the walls, which represent the solidification front. The capture of inclusions by an advancing solidification front involves complex phenomena which have been investigated in many previous studies, which have been reviewed elsewhere [57]. Particles that are smaller than the dendrite arm spacing are captured if they touch the interface. However, larger particles may be pushed along by the moving front unless the solidification exceeds a

critical velocity to engulf them. To model these important larger particles, fundamental capture criteria are being developed as part this project. In addition to the forces considered in previous work, this work is incorporating two important phenomena which have not been previously investigated. These are: 1) The interface of interest is dendritic, rather than the flat front assumed in previous work. 2) Flow across the dendritic front generates additional forces that make inclusion capture more difficult. The effects of critical dendrite growth velocity, particle size, primary dendrite arm spacing (PDAS) and local cross-flow velocity all are being considered [57].

The results presented here focus on particles smaller than the PDAS which can easily enter in between primary dendrite arms and become entrapped with little chance of being pushed away regardless of solidification front velocity [57]. Measurements on the caster of interest here (**Fig. 2**) [58] show that the PDAS is smallest near the top surface (about 50μm) and increases along the casting direction as the solidification rate slows. Thus, this work investigates 10μm and 40μm particles which are predicted to become entrapped instantly upon touching the solidification front.

(iv) Solution Procedure

The particle transport equations were integrated using the fourth order Runge-Kutta method [59]. Particle velocities and displacements were solved at every time step after the fluid velocity field was solved. The local fluid velocity in the drag and lift terms of Eq.[2] was interpolated from the nearest neighbor cells using a second order scheme [59]. Due to the low volume fraction of impurity inclusions for the continuous casting process (~0.01% for a typical steel with 30ppm oxygen), one-way coupling was employed, which neglects the modification of fluid turbulence by the particles. The removal and capture criteria were tested whenever a particle crossed a domain boundary.

(v) Computational Details

In this work, the transport and capture of four groups of 10,000 small inclusions, with two different sizes (10μm and 40μm) and two different densities (2700 kg/m^3 and 5000 kg/m^3), were simulated in an thin slab steel caster (Fig. 1). These inclusions could represent entrained mold slag or alumina particles, with varying amounts of entrained steel filling internal voids and thus raising its density. The computational domain has two portions. The nozzle domain includes part of the bottom of the tundish and the entire 1.11m long trifurcated submerged entry nozzle. The strand domain includes the top 2.4m of the molten pool in the mold and strand. This 2.4m computational domain is part of the 3m straight section of the

caster. In contrast with the water model, the steel caster has no solid bottom wall. The internal liquid pool domain shape was curved to account for the shell, and had mass flowing through it to represent solidification. The shell thickness increases from 0 at the meniscus to 26mm (wide face) or 25mm (narrow face) at domain exit [53]. The two different densities assigned to the particles represent different fractions of molten steel in the inclusion. [60] The 40,000 computed particles were introduced into the three nozzle port outlet planes over 9s (33-42s of the fluid simulation). More information on casting conditions, material properties and computational parameters on both cases is given in Table I. Methodologies were implemented to optimize the time step size and computational cost, according to the particle response time. Both the flow simulations (1.3M cells) and the transport of 40,000 particles took about 29.2 CPUs per fluid time step (0.001s).

B. Model Validation in a Full-Scale Water Model

The computational model of particle transport was first applied in a full-scale water model, where measurements on particle removal are available. [32] In the experiments, around 8,000-30,000 elliptical disk-shaped plastic beads were injected into the liquid pool with water through the nozzle over a few seconds. [32] The density and size of the beads were chosen to aid visualization while approximating the vertical terminal velocity expected of typical 300μm inclusions in liquid steel. [32] To model the removal of inclusion particles to the top surface, a screen was positioned near the top surface and the SEN to trap plastic beads as they flowed across the top surface towards the SEN and headed downwards. The experiments were repeated at least five times and the average inclusion removal fraction by the screen was reported elsewhere. [32]

In the simulation, the fluid velocity field was solved using LES [53]. The capture of particles by the screen was modeled by summing the particles that crossed the screen from the top. The screen influenced neither the fluid velocity field [53] nor the particle transport. The particles were divided into five groups of 500 particles and another six groups of 2,500 particles, in order to investigate statistical variations and the effect of the number of particles. The particles were injected into the nozzle ports over a realistic time interval.[54]

The particle fractions removed by the screen for the 2,500 and 500 particle groups are presented in Table II, and are also compared with measurements. The average removal fractions for both groups agree with experiments within ±5%. However, the removal fraction varies greatly between groups, especially for the first 10s after particles enter the mold. This is reflected by the standard deviation,

($\sigma_u=\sqrt{\sum_{i=1}^{N}(u_i-u_{mean})^2/N}$) which decreases from 5.5% (500 particle groups) and 4.8% (2,500 particle groups) for 0-10s to 2.9% and 1.4% for 10-100s. The standard deviation of the 2,500 particle groups is always lower than that of the 500 particle groups, as expected due to the improvement in statistical confidence with increasing population size. However, the improvement is small for 0-10s. This suggests that during early times, particle removal is chaotic, because it is dominated by the turbulent eddies of the initial jet. To obtain a more reliable statistical estimate of the mean would require injecting particles during different time intervals. Increasing the number of particles improves the statistics at later times, (e.g. 10-100s) because the standard deviation drops in half. This is because the particles become well dispersed in the liquid pool and random statistics become valid.

C. Results of Particle Transport and Entrapment in the Thin-Slab Caster

After examining the accuracy of this computational model of particle transport in a standard-slab water model, it then was applied to investigate the transport and capture of small inclusions in the actual thin slab steel caster (Fig. 1), in which a trifurcated nozzle is used [16, 54, 58]. The fluid velocities were obtained from LES [53] and conditions are given in Table I.

(i) Particle Removal and Capture Fractions

The removal and capture history in the strand of the four groups of particles of different sizes and densities are compared in **Fig. 3** and Table III. Particles exiting the nozzle ports could touch the outer nozzle walls, reach the top surface of the liquid pool to be removed, or become entrapped either by touching the solidification front (sides) or exiting the domain bottom. All four different types of particles in Fig. 3 have approximately the same capture and removal histories. Thus, the statistics in Table III are independent of particle size and density. This is expected because the small buoyancy force relative to drag for these small particles (≤40μm), as indicated in Eq. [2] produces small terminal velocities (≤0.65mm/s) relative to the fluid.

Approximately 8% of the particles that exit the nozzle ports are seen to be removed by the top surface. A further 8% of the particles touched the outside of the nozzle wall while recirculating in the liquid pool and might be removed, depending on the inclusion composition and nozzle properties. Most (90%) of these particles reached the surface within 47s (Fig. 3). Most (90%) of the captured particles flowed for less than 72s. The final statistics (Table III) were compiled after all particles exiting the

nozzle ports were either removed or captured, which took approximately 220 seconds. Approximately 51% of the particles were captured by the shell in the upper 2.4m of the strand where the shell thickness was less than 25mm (narrow face) or 26mm (wide face). Around 32% of the particles exited the domain from the bottom and would be captured at a deeper (and more interior) position in the solid slab. These results suggest that most (84%) of the small inclusions which enter the mold become entrapped in the final product. Thus, nozzle design and mold operation should focus on controlling flow at the meniscus to avoid the entrainment of new inclusions rather than altering the flow pattern to encourage removal of inclusions entering the mold. This conclusion may differ for large inclusions or if gas bubbles are present.

(ii) Inclusion Capture in Solid Steel Slabs after a Sudden Burst

A sudden "burst" of inclusions entering the liquid pool may occur in the continuous casting process during upstream events such as temporary vortexing, release of a nozzle clog or other upset. [61, 62] Knowledge of the inclusion distribution in cast steel slabs caused by such a burst is important for the subsequent inspection and dispositioning of the product. The particle study in this work can be considered as a 9s burst of 40,000 inclusions entering the molten steel pool. By relating the total time traveled by each particle with the casting speed and its capture position, the distance of each of the 51% of the captured particles down the final solidified slab was calculated. The final positions of these particles are shown in **Fig. 4**, as transverse projections onto the wide and narrow faces. Zero on the vertical axis points to the slice of the shell which was at the meniscus at the time when the first particle entered the strand (33.0s). All slices continuously moved downward with the whole shell at the casting speed during the process. The shadowed length in Fig. 4 is the distance traveled by the strand during the 9s burst. The simulation shows that the 220 seconds needed for all 51% particles to be captured corresponds to a length of around 7m. Most (78.5%) of those particles were captured within 1m above and below the zero-slice. Only a slight asymmetry of the capture positions can be observed from both view angles. This indicates that the flow asymmetries discussed earlier are not significant relative to particle capture. The great asymmetries observed in practice [63] must have been caused by extreme flow asymmetries involving transient events such as a slide gate opening change, or asymmetrical release of a nozzle clog or gas accumulation. Such events were not considered in this study, but are investigated elsewhere. [23]

(iii) Total Oxygen Distribution in Thin Steel Slabs

Total oxygen is often measured to evaluate the content of oxidized inclusions such as alumina in steel slabs. [41] It can also be calculated based on the computed positions and times of particle capture. The distribution of particles captured under a condition of continuous injection is found from the results in the previous section by assuming the 9s burst of particles to repeat every 9 seconds. The molten steel was assumed to exit the nozzle with a steady oxygen content of 10ppm (by mass), from pure alumina (Al_2O_3) inclusions. The oxygen distribution in a typical cross section through the solidified slab was obtained by first projecting the entire computational domain [54] onto a transverse x-y section to define a 2-D grid of 3-D cells. The cell transverse dimensions, Δx and Δy, vary from 0.5mm to 6mm according to distance beneath the strand surface. The cell vertical dimension, Δz, is the length cast, 228.6mm, during the 9s burst. The total oxygen concentration in each cell, C_O, was calculated by dividing the mass of oxygen in all particles entrapped in that cell by the cell mass (including both cast steel and particles):

$$C_o = \frac{(48/102)\, M_p}{\rho(\Delta x \Delta y \Delta z) + (1-\rho/\rho_p) M_p} \qquad [7]$$

where $M_p = \sum_{i=1}^{N_C} \frac{\pi d_p^3 \rho_p}{6}$ and N_c are the total mass and number of particles entrapped in the cell. The central region representing the area of the liquid pool at the domain exit was treated as a single large cell. This cell would contain all of the inclusions that exited the domain.

The number of particles entrapped in each cell, N_C, was obtained by summing the contributions from a series of 9s bursts. Each burst represents the contribution from a different time interval. The entrapment locations for each burst are obtained by translating the results in Fig. 4 vertically by Δz*i. The burst number i is an integer with a minimum value from the z coordinate of the last particle captured (-5.2m from Fig. 4) divided by Δz. The maximum i value is the domain bottom coordinate (+1.9m) divided by Δz. The final particle distribution is obtained from the sum of the entrapment distributions from each value of i within this range.

The results are given in the cross section of the steel strand shown in **Fig. 5**. The dashed line represents the boundaries of the central large cell and is the solidification front at the domain exit (2.4m below meniscus). The highest total oxygen content (about 170ppm) is predicted near the corners, closely followed by intermittent patches on the narrow faces. Intermittent patches with high oxygen

concentrations (50-150ppm) are also found in the middle region of the strand (approximately 10-20mm beneath the slab surface). These results indicate that most of the captured particles (69%) are entrapped within the shell approximately 0.4-1.5m below meniscus (corresponding to a shell thickness of 10-20mm).

The finding of increased inclusion capture across the slab width towards the narrow faces agrees with previous measurements [32] and calculations [64] Other measurements find sliver defects concentrated at the surface more towards the wide face centerlines. This is only a slight trend here, owing to impingement from the bottom central port. More severe centerline concentrations would have been predicted if some of the inclusions hitting the top surface were able to continue moving with the flow towards the SEN before being captured in the steel shell at the meniscus. Alternatively, the larger particles which contribute the most to sliver defects have more complex entrapment criteria, such as being pushed along at the solidification front before capture.

Figure 6 reveals the oxygen content along the two centerlines shown in Fig. 5. Higher inclusion concentrations are found towards the surfaces. Similar variations in total oxygen distribution have been measured in other steel slabs, in which particles were found to concentrate most within 20mm of the slab surface. [46] Small regions with high oxygen content are also distributed sparsely towards the center of the wide faces. This is caused by groups of particles from the center nozzle port. Small patches with low total oxygen close to zero are randomly distributed in the cross section, indicating the effects of turbulent motion of the fluid. Asymmetries can be observed in this symmetrical domain, confirming the influence of fluid instabilities on particle transport and capture. No significant difference is observed between the inside and outside radius, which is consistent with the lack of buoyancy of the small particles considered in this work. In practice, large inclusions are generally of more relevance to quality problems, so future work will focus on developing a capture model for large particles.

D. Conclusions

Lagrangian computations of particle transport during continuous casting of steel slabs were performed in this study. Time-dependent fluid velocity fields obtained from LES were employed in the particle computations. The computational model was applied to simulate the transport and capture of 10μm and 40μm inclusions in a thin slab steel caster. The present study confirms the importance of flow transients in affecting the transport and capture of inclusions during continuous casting.

The following conclusions are reached, based on the results of this study:

(i) A comparison of particle removal fractions obtained from 2,500 and 500 particle groups suggests that increasing the number of particles improves the accuracy of removal predictions, for later times (e.g. 10-100s). At least 2500 particles are required to obtain accuracy within ±3%. Particle removal at early times (e.g. ≤10s) is governed by chaotic fluctuations of the flow, which generate variations of ±5%.

(ii) The top surface is predicted to remove only 8% of small particles (10μm and 40μm) in the thin slab steel caster. An equal fraction touches the outside of the nozzle walls in the mold. These removal fractions are independent of both particle size and density, owing to the inability of the small, low-buoyancy particles simulated here to deviate significantly from the surrounding fluid flow.

(iii) The computation shows that after a 9s sudden burst of particles enter the steel caster, about 4 minutes are needed for all of them to be captured or removed, for the casting conditions assumed here. The captured particles concentrate mainly within a 2-m long section of slab.

(iv) With a steady oxygen content of 10ppm from inclusions in the molten steel supplied from the nozzle ports, intermittent patches of high oxygen content (50-150ppm) are found concentrated within 10-20mm beneath the slab surface, especially at the corner, and towards the narrow faces.

Table I. Properties and conditions of the particle simulation in the thin-slab steel caster.

Parameter/Property	Thin-Slab Caster	Full-Scale Water Model
Mold Width (mm)	984	1830
Mold Thickness (mm)	132	238
Water Model Length (mm)	-	2152
Mold Length (mm)	1200	-
Domain Width (mm)		
- top	984	915
- bottom	934.04	915
Domain Thickness (mm)		
- top	132	238
- bottom	79.48	238
Domain Length (mm)	2400	2152
Nozzle Port Height × Thickness (mm × mm)	75 × 32 (inner bore)	51×56
Bottom nozzle Port Diameter (mm)	32	-
SEN Submergence Depth (mm)	127	150
Casting Speed (mm/s)	25.4	15.2

Fluid Dynamic Viscosity (m^2/s)	7.98×10^{-7}	1.0×10^{-6}
Fluid Density (kg/m^3)	7020	1000
Particle Density (kg/m^3)	2700 and 5000	988
Particle Diameter (μm)	10 and 40	3800

Table II. Comparison of fractions of particles removed by the screen in the water model.

		0-10 seconds	10-100 seconds
LES	**500 particle groups**		
	1	27.2%	23.4%
	2	17.8%	27.2%
	3	26.2%	23.0%
	4	23.8%	23.2%
	5	33.0%	18.2%
	Average	**25.6%**	**23.0%**
	Standard Deviation	5.5%	2.9%
	2500 particle groups		
	1	27.2%	25.9%
	2	26.8%	27.1%
	3	20.0%	26.5%
	4	23.3%	27.8%
	5	31.8%	24.1%
	6	32.6%	24.9%
	Average	**27.0%**	**26.1%**
	Standard Deviation	4.8%	1.4%
Experiment		**22.3%**	**27.6%**

Table III. Statistics of particle entrapment and removal obtained from thin-slab caster simulation.

		Group 1	Group 2	Group 3	Group 4	Average
Diameter (μm)		40	40	10	10	-
Density (kg/m^3)		5000	2700	5000	2700	-
Fraction of	Captured by shell	51.58%	51.51%	50.79%	51.00%	51.22%
	Captured deeper	32.22%	32.07%	32.77%	32.54%	32.40%
	Removed by top surface	8.03%	8.49%	8.23%	8.20%	8.24%
	Removed by nozzle wall	8.12%	7.83%	8.03%	8.15%	8.03%

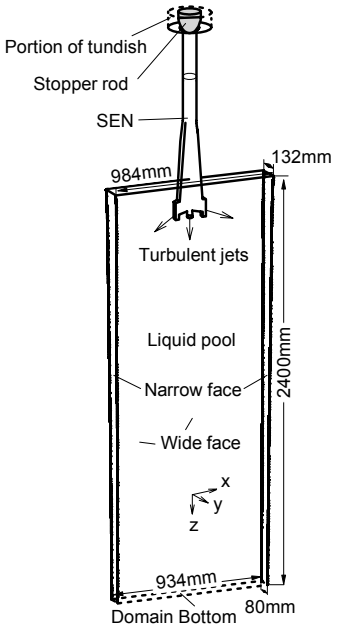

Fig. 1. Schematics of the computational domain of the thin-slab steel caster.

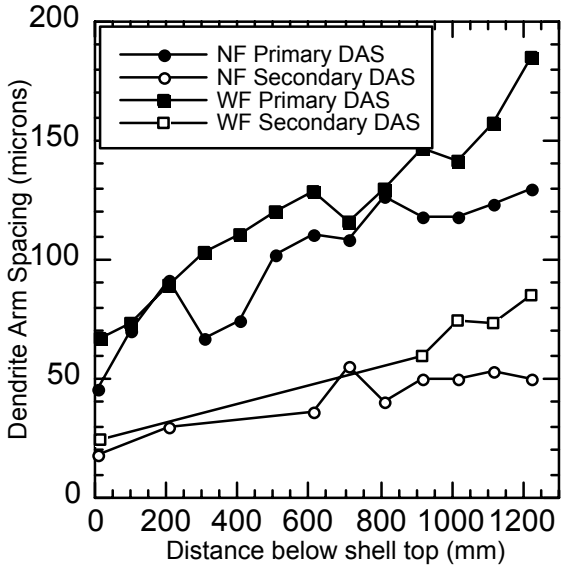

Fig. 2. Variation of primary dendrite arm spacing (PDAS) along distance below meniscus. [58]

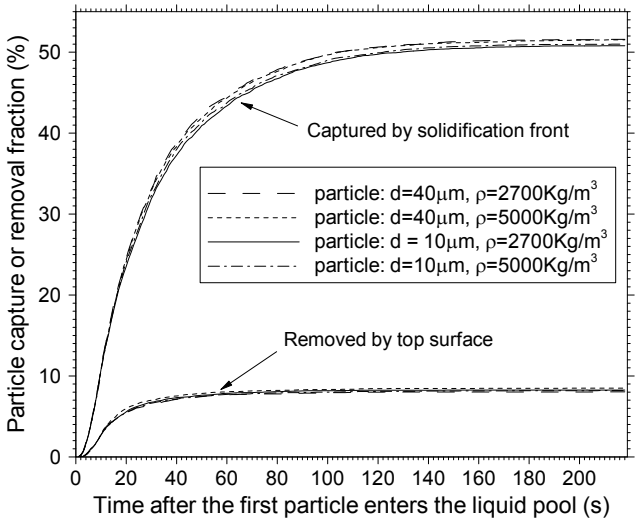

Fig. 3. Predicted particle removal and entrapment history in the thin-slab steel caster.

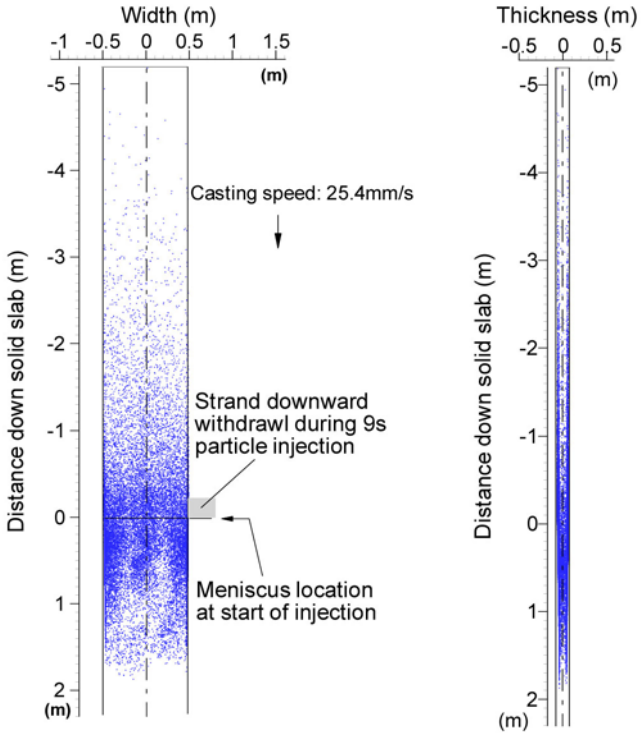

Fig. 4. Particle entrapment location for 9s injection: projection onto the wide face (left) and the narrow face (right).

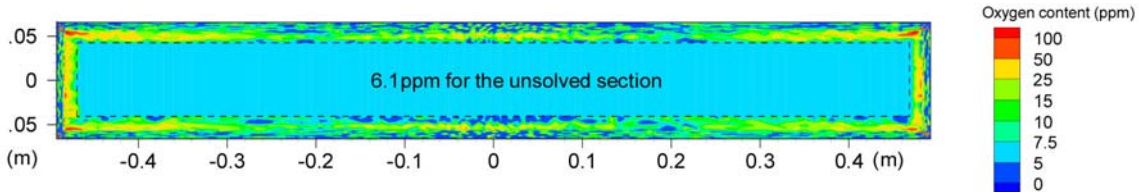

Fig. 5. Predicted oxygen concentration averaged in the length direction (10ppm oxygen at nozzle ports).

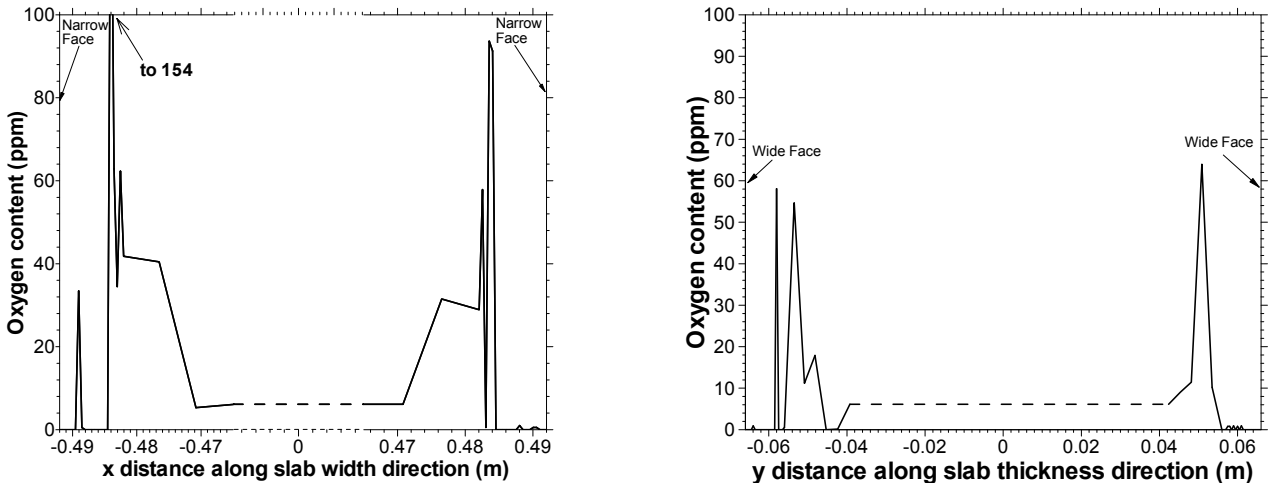

Fig. 6. Oxygen content along the centerlines in Fig. 5.

5.2 Parametic Study: Effect of Nozzle Geometry On Inclusion Entrapment

Inclusion removal is affected by many parameters which affect the flow pattern in the mold cavity, including the nozzle and mold geometry, submergence depth, steel flow rate, argon injection rate, electromagnetic stirring, and flux layer properties. Changing nozzle geometry is an easy and inexpensive way to optimize the fluid flow in the mold. Technologies to improve fluid flow and inclusion removal involving the Submergence Entry Nozzle (SEN) include the nozzle port angle, introduction of flow directors that create swirl, multiple outlet ports, throttling plates with oval offset bore, and internal horizontal steps to introduce turbulence. The nozzle port angle and the step nozzle technique [65] are investigated here.

Steady flow in the strand of the continuous caster is simulated with a 3-D finite-difference computational model using the standard k-ε turbulence model in Fluent [54, 66]. Inclusion trajectories are calculated by integrating each local velocity, considering its drag and buoyancy forces. The "random walk" model is used to incorporate the effect of turbulent fluctuations on the particle motion. As boundary conditions for the particle motion, particles escape at the top surface and the open bottom, are reflected at the symmetry plane, and are entrapped when they touch the wide faces and narrow faces, which represent the dendritic solidification front. This entrapment condition was shown to be valid for particles smaller than the primary dendrite arm spacing [57]

The effect of steps in SEN and the outport angle of SEN on the fluid flow and particle motion in the mold is investigated. The parameters of the caster are shown in Table IV.

A. Comparison of Inclusion Removal between Simulation and Industrial Measurements

The distribution of inclusions along the slab thickness measured from microscope observations is shown in **Fig. 7**, which suggests that: 1). Inclusions concentrate more in the 20mm thickness nearest the slab surface; 2). Some slabs have occasional accumulation at the ½ and the ¼ slab thickness from the inner radius; 3). Filters in the tundish are effective at lowering microinclusion levels. Further investigation indicates that this inclusion accumulation is more prevalent in places such as the slab head and tail cast during unsteady conditions. Microscope observation and SEM detection suggest that this inclusion accumulation is mainly induced by the entrapment of dislodged clogged materials from the SEN during the ladle change. Slag inclusions are mainly entrapped at the surface of the slab. The inclusions mass fraction is 66.8ppm in the tundish, 57.7ppm in the 20mm thickness nearest the slab surface, and averaging 51.9ppm in the slab. This suggests that inclusions in the interior of the slab (i.e.,

except outer 20mm thickness of the slab) is 50.6ppm. The fraction of inclusions removed from tundish to slab is around 22%.

Computed locations of inclusions that attach to the SEN walls and are entrapped at the wide faces of the slab and inclusion measurement are shown in **Table V**. The calculation suggests that around 12% of the inclusions leaving the tundish stick to the SEN walls (removed by clogging). The buildup is roughly uniform on the nozzle walls, with increased tendency towards buildup on the SEN bottom due to impact from the flowing jet. This is consistent with observations of nozzle clogging where local reoxidation or chemical interaction were not the cause.

For inclusions smaller than 50 μm entering the mold, only 7% are safely removed by the top surface (6% from tundish to slab), independent of inclusion size. A larger fraction of inclusions bigger than 50 μm are removed. The majority of inclusions leaving the tundish (more than 60%) are captured within 30mm of the surface, which represents the top 2.55m of the caster. Fig. 7 also shows that inclusions accumulate peaks are at 12-14mm below the surface of the slab. This agrees only qualitatively with measurements in Fig. 7. A disproportionately large fraction of these (15-16%) are captured in the narrow face, despite its smaller surface area, owing to the jet impingement against its inner solidification front. Inclusions exiting the domain are entrapped somewhere deeper in the interior than 30mm shell thickness.

If the entrapment criterion is the same for small and large inclusions, then their entrapment behavior is similar. (This assumption will be refined in future work). Only 3-12% of the inclusions entering the mold are predicted to be removed by the top surface (2.6-11% from tundish to slab). Adding 12% sticking to the SEN walls as clogged material, the simulated inclusion removal from tundish to slab is 18-23%, which agrees with the measurement of 22%.

Although this relatively simple model still needs to be validated rigorously with the more refined LES model, this aproximate agreement is encouraging. Both experiments and models suggest that the removal rate of small inclusions in the mold is quite small.

B. Effect of SEN Port Angle and Steps on Flow and Inclusion Removal

Due to the sharp decrease of the bore diameter at the steps, the fluid flow is accelerated at these locations in the Step SEN. This acceleration helps to diminish the non-uniform velocities generated by the slide gate, as shown in **Fig. 8** (center). Without steps, the uneven flow passing the slide gate eventually generates a swirl at the bottom of the nozzle and in the jets entering the mold. This swirl is diminished in the Step SEN. Jet characteristics for nozzles with outports angle of 15^o down, 0^o horizontal, 15^o up, and Steps are compared in **Table VI**. The 15^o down nozzle with two steps has the smallest turbulent energy and dissipation rate, which means the jet entering the mold has the weakest turbulence. The jet angle is only 18^o down for the Step SEN (15^o down), compared with 29^o without steps (15^o down), and 18^o for Zero degree angle nozzle without Steps. The large jet angle causes a deep impingement point, which lessens inclusion removal to the top surface. One problem of the Step SEN is its large back flow zone fraction, 30%, compared with all three conventional nozzles in Table VI. The larger back-flow zone will bring more inclusions back to the outport region of SEN, possibly inducing clogging there.

All four nozzles investigated have a classic double roll flow pattern for these conditions of deep 300mm submergence and no gas injection. The upper loop reaches the meniscus and may increase the surface height near the narrow face. The lower loop takes steel downwards into the liquid core where it eventually flows back towards the meniscus in the strand center. However, the impingement point on the narrow face and the jet penetration depth is different. Without steps, the penetration depth is deeper than with steps. The steepest nozzle angle naturally produces the deepest penetration depth. Results indicates that annular steps in the SEN decreases the penetration depth. The eye of the lower loop with steps is higher than without.

The fraction of inclusions transported to different destinations are shown in **Table VII**. For the current domain length 2.55m, and the current casting speed 1.2m/min (0.02m/s), the shell thickness at the open bottom of the domain is around 30mm, based on solidification model results [42]. Of the 50 μm inclusions entering the mold, 31.4% are predicted to be entrapped in the central region of the slab (30-125mm thick) using the non-step 15o down nozzle. This number decreases to 15.7% for the stepped 15o down nozzle, 17.1% for the zero angle nozzle, and 29.4% for the 15o up nozzle.

For the down 15^{o} angle nozzle, only 3% of the inclusions are removed to the top surface, but this number increases to 7% with two annular steps. The step nozzle is predicted to have slightly more inclusion removal to the top surface of the mold, perhaps by eliminating swirls at SEN outports and in the mold, and deceasing the impingement depth of the jet in the mold. Table VII also shows that a disproportionate number of inclusions are entrapped by the narrow faces (18%) compared with the wide faces (50-60%). From the average residence time of inclusions prior to entrapment, the positions of inclusion accumulation peaks near the surfaces of the slab can be calculated. The results indicate that inclusions accumulate at 12-14mm below wide surfaces, and 9-10mm below the narrow surfaces. Because the inclusion removal rates are so small for all nozzles, it is more important to choose nozzle designs that produce optimal conditions at the meniscus to avoid slag entrainment, level fluctuations, and other problems.

C. Summary

Measurement indicates that trapped inclusions concentrate mostly within 20mm of the slab surface. Some slabs have occasional concentration at the ¼ slab thickness from the inner radius, mainly induced by the entrapment of released clogged materials from the SEN during ladle exchanges. In the continuous caster, around 12% of inclusions leaving the tundish are removed by sticking to the SEN walls, and only 3-11% are predicted to be removed to the top slag of the mold. This roughly matches the measured total inclusion removal fraction to the top surface of 22%. The majority of simulated inclusions entering the mold (60%) are captured within 30mm of the surface of the slab, which represents the top 2.55m of the caster. Simulation indicates that inclusion accumulation peaks are at 12-14 mm below the surface of the wide face, which agrees well with the measurement.

Table IV. Parameters of the caster

Parameters	Value
Inlet port size (width×height) (m×m)	0.065×0.080
Nozzle angle	Down 15^{o}, up 15^{o}, zero
Submergence depth (m)	0.3
Domain height/width/thickness (m)	2.55/1.3/0.25
Average inlet flow rate (half mold) (m^3/s)	0.00325
Casting speed (m/min)	1.2
Fluid density (kg/m^3)	7020
Fluid kinetic viscosity (m^2/s)	0.954×10^{-6}
Particle density (kg/m^3)	5000
Particle diameter (μm)	49, 225

Inlet condition	Nozzle simulation result
Gas flow rate	None
Turbulence model	k-ε, by Fluent
Inclusion motion model	Random walk model, Fluent, 80 tries, 16000 inclusions
Boundary condition for inclusions	Escape from top surface and open bottom, trapped at narrow and wide face walls

Table V. Fractions of inclusions entrapped at different locations after leaving tundish

Simulation	Size	SEN walls	Top slag of mold	Slab		
				Narrow face	Wide face	Interior
				0-30mm	0-30mm	30-125mm
	50μm	**12%**	**2.6-6.9%**	15-16%	40-43%	15-28%
	225μm	**12%**	**11%**			
Measurement	All	**22%** (decrease from tundish to slab)				

Table VI Jet characteristics of SEN with different outport angles or SEN steps

SEN Outport angle	Down 15	Down 15	Zero	Up 15
With steps or not	No	Two Steps	No	No
Weight average x velocity (m/s)	0.80	0.96	0.87	0.86
Weight average y velocity (m/s)	-0.0351	0.012	0.0018	-0.007
Weight average z velocity (m/s)	0.45	0.32	0.14	0.28
Weight average turbulent energy (m^2/s^2)	0.27	0.20	0.32	0.31
Weight average turbulent energy dissipation rate (m^2/s^3)	6.41	5.27	10.47	8.88
Vertical jet angle (^{o})	29.29	18.23	9.10	17.76
Horizontal jet angle (^{o})	-2.52	0.72	0.12	-0.47
Jet speed (m/s)	0.92	1.01	0.89	0.90
Back-flow zone fraction (%)	15.31	29.38	26.15	20.73
With swirl or not at Outports	With	No	With	With

Table VII Inclusion fractions to different destinations, and average residence times before entrapment

	Fractions to different destinations (%)						Average residence times (s)				
	Top	Wide1	Wide2	Narrow	Bottom		Top	Wide1	Wide2	Narrow	Bottom
Down15^o	2.9	20.5	27.5	17.6	31.4		23.7	23.9	22.5	13.5	25.9
Down15^o (Steps)	6.9	28.9	30.3	18.2	15.7		11.1	23.6	26.1	13.0	49.1
Zero	5.1	23.5	35.8	18.4	17.1		22.7	26.7	20.4	14.8	31.7
Up15^o	2.8	20.4	28.0	19.3	29.4		21.7	41.7	33.3	19.5	54.5

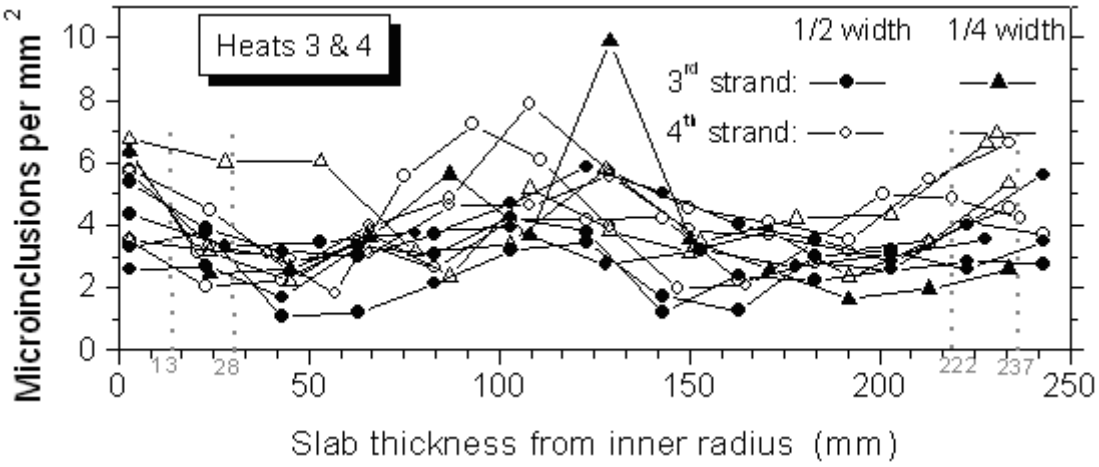

Fig.7 Inclusions distribution (<50μm) along the slab thickness with (strand 3) and without (strand 4) tundish filters

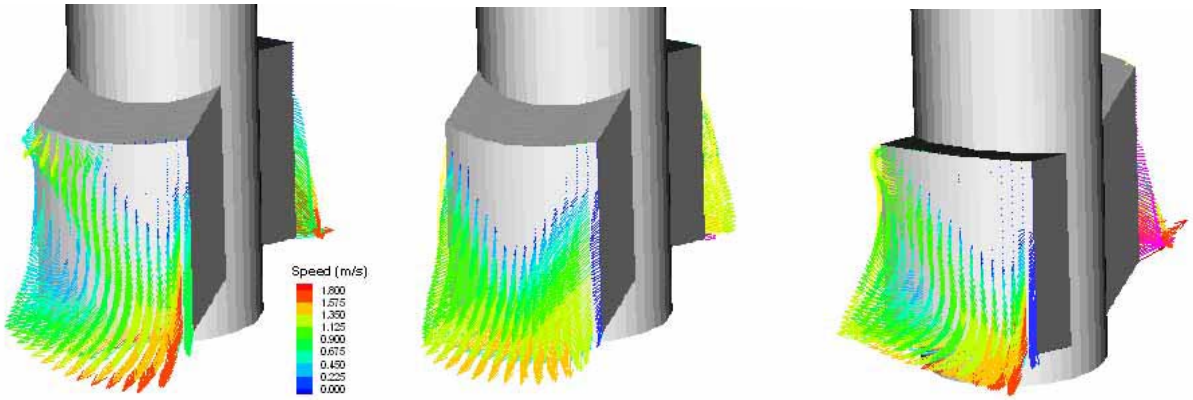

Fig. 8 Flow pattern at outports of 15° down angle without steps (left), 15° down angle with steps (middle), 15° up angle without steps (right)

5.3 Nucleation and Growth Models for Inclusions in Molten Steel

Inclusion size and number distribution is greatly affected by collisions with other inclusions, and varies continuously during processing, so tracking the evolving size distribution during the flow process is desirable. A model has been developed to predict inclusion size distribution evolution and applied to a ladle [37, 39, 51]. In addition to being a simple test system for model development, inclusion removal from ladles is of critical importance in removing inclusions from the final product, as the previous results have shown that it is very difficult to remove many of the inclusions that enter the mold.

It is best to start the model from nucleation, in order to avoid uncertainties in initial conditions. There are serious computational issues involved in solving the classic population balance equation of

inclusions. These are the computation time and the array limit for memory storage. Because the model is being designed to simulate nucleation (concerned with individual molecules with sizes on the order of nanometers) up to collision of real particles (on the order of microns), the particle size range varies over 3 orders of magnitude, and contains from 1 to ~10^{13} molecules per particle. Using classic population balance equation of inclusions with a simple linear scale becomes prohibitive for this real system. To make this difficult problem feasible, a simplified model that can accurately handle varying size ranges — Size Group Model — is employed. In this model, the inclusions are divided into groups (group number k) with average particle volumes related by the following ratio:

$$\frac{V_k}{V_{k-1}} = R_V \qquad [8]$$

where $2<R_V<3$ with 2.5 a typical value. The method can be developed for other choices of R_V, but the following equations change slightly. Considering the critical size group j_c for a stable particle, the evolution equations become:

① $2 \le j < j_C$ (namely nucleation)

$$\frac{dN_j}{dt} = N_j \beta_j^D N_1 \frac{V_1}{V_j} - \alpha_j A_j N_j \frac{V_1}{V_j} \qquad [9]$$

② $j \ge j_C$ (namely growth)

$$\begin{aligned}\frac{dN_j}{dt} = {} & N_j \sum_{k=1}^{j-1} \left(\phi_{kj} \left(\beta_{kj}^T + \beta_{kj}^B \right) N_k \frac{V_k}{V_j} \right) + \phi_{j-1.j-1} \left(\beta_{j-1,j-1}^T + \beta_{j-1,j-1}^B \right) N_{j-1} N_{j-1} \frac{2V_{j-1}}{V_j} \\ & - \sum_{k=j}^{j_{\max}-1} \left(1+\delta_{jk}\right) \phi_{jk} \left(\beta_{kj}^T + \beta_{kj}^B \right) N_j N_k \\ & + N_j \beta_i^D N_1 \frac{V_1}{V_k} - \alpha_j A_j N_j \frac{V_1}{V_j}\end{aligned} \qquad [10]$$

where β_i^D is The rate constant for pseudo-molecule diffusion, β_{ij}^B represents Brownian collision and β_{ij}^T represents turbulent collision, based on Saffman's model [67].

According to classical homogenous nucleation theory, the critical radius of nucleus r_C is

$$r_C \equiv \frac{2\sigma V_m}{RT \ln \Pi}. \qquad [11]$$

If $r > r_C$, nucleation occurs, and stable particles precipitate and start to grow. According to Eq.[11], the critical size of nucleus decreases with increasing supersaturaion Π and decreasing surface tension. If j_c is the critical group number, beyond which nucleation occurs, j_c can be represented by

$$j_c = 1 + \frac{3}{\ln R_v} \ln\left(\frac{2\sigma V_m}{RTr_1} \frac{1}{\ln \Pi} \right)$$

(5)

The supersaturation of free Al_2O_3 molecules, Π, is represented by

$$\Pi \equiv \frac{N_1}{N_{1,eq}}, \qquad [12]$$

where $N_{1,eq}$=2.634×1023 m^{-3} corresponds to 3ppm dissolved oxygen in steel at equilibrium. The total number of Al_2O_3 molecules including those in nucleated inclusions (NS), which is a function of dimensionless time, represented by Eq.[12] from the calculation of aluminum dissolution and diffusion in molten steel, which defines how fast the Al_2O_3 molecules appear and disperse in the liquid steel after the deoxidizer-Al is added.

$$N_S^* = 100\left[1.0 - \exp\left(-\frac{t^*}{10} \right) \right], \qquad [13]$$

This equation was used in modeling inclusion evolution in a ladle [39].

B. Ladle Mixing Times

Aluminum is added into molten steel from solid aluminum to melt and dissolve into free aluminum atoms. Once the solid aluminum is dissolved, the aluminum atoms are available to react with the free oxygen in the molten steel to generate alumina inclusions. The calculated nucleation time is in the order of 1μs, which is very fast compared with the mixing of aluminum atoms in the molten steel. **Figure 9** shows the aluminum dispersion in an argon stirred ladle of molten steel, which indicates that the mixing process is much slower, roughly 10^8 times slower than the nucleation process. The mixing time is defined as the time at which the mass fraction reaches 95% of the infinite average fraction. The calculated mixing times vary greatly at different points in the ladle, as shown in **Fig. 10**. Within this

uncertainty, the computations in figure 10 agree with previous measurements [68]. Increasing stirring power naturally decreases the mixing time. Inclusion trajectories in this argon-stirred ladle also shown in **Fig. 11**, which indicates a long moving path length before inclusions reach the top surface to be removed.

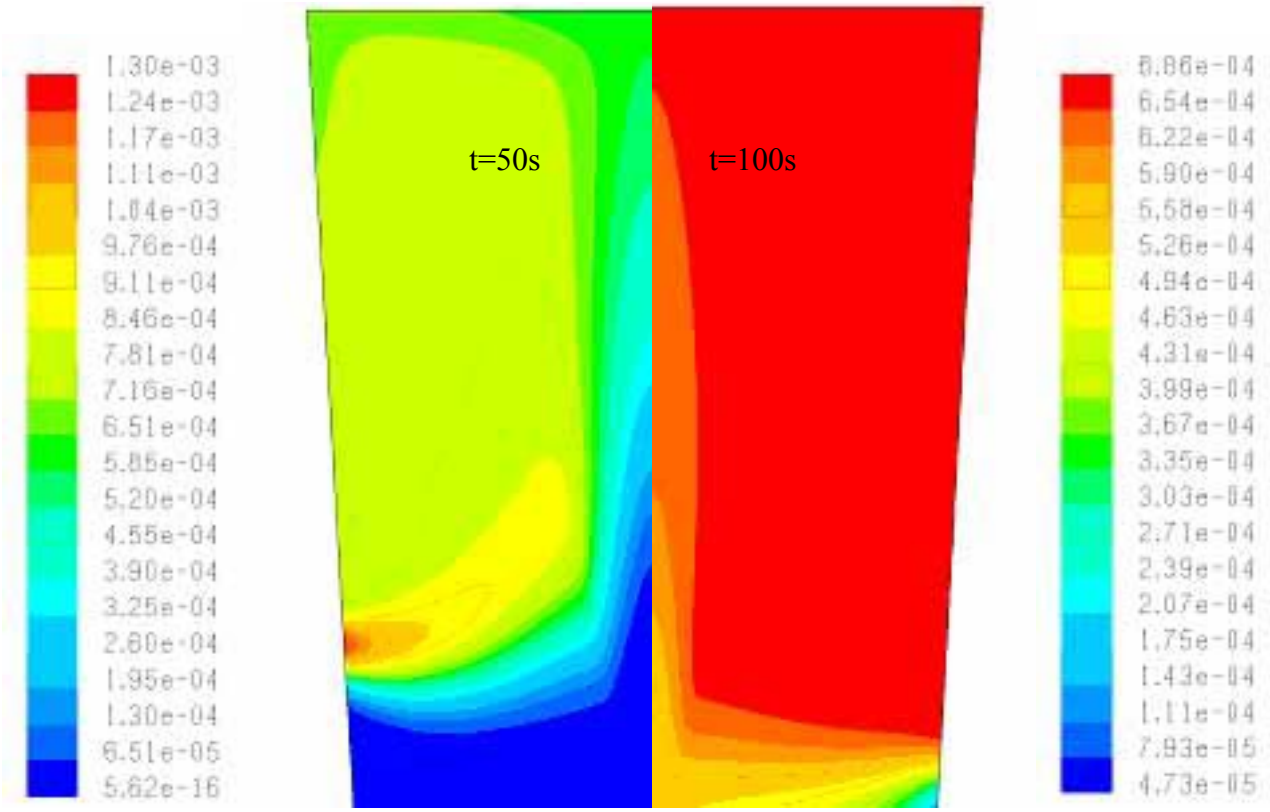

Fig.9 Aluminum mass fraction distribution in ladle at different time

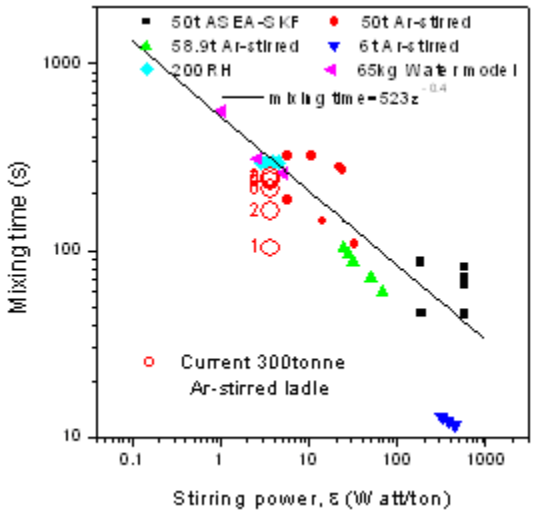

Fig.10 Mixing time deceasing stirring power

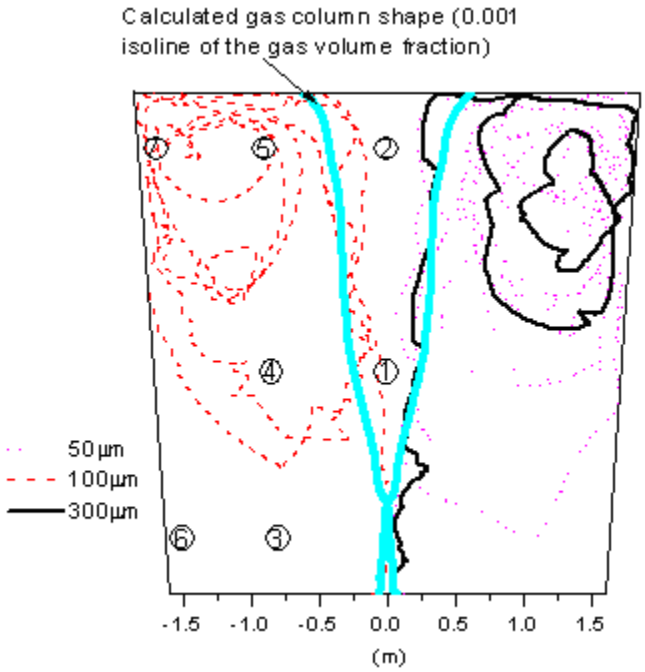

Fig.11 Inclusion trajectories in argon stirred ladle

5.4 Flow and Heat Transfer in a Molten Flux Layer

Flux is added to the top of molten steel in the mold, where it melts to form a liquid slag or "flux" layer, which absorbs inclusions, and also acts as an insulator from heat loss through the top surface. This latter function is important to superheat transport and temperature near the meniscus, where hooks can trap inclusions if they are allowed to solidify.

Numerical simulations have been performed to study coupled fluid flow and heat transfer in a thin liquid slag or flux layer [55]. The combined effects of natural convection, bottom shear velocity and strongly temperature dependent viscosity are investigated. The steady-state Navier-Stokes equations are solved using the commercial finite volume code FLUENT.

The code was validated against analytical solutions as well as natural convection experiments in literature [55], excellent agreement was achieved in all cases. Computations are performed for several different commercial fluxes and bottom shear velocities.

The flux layer is approximated as a two-dimensional rectangular domain with a length of 0.7 m and thickness of 0.01 m. This depth often varies from the narrow face to the submerged entry nozzle, according to the flow pattern of the molten steel beneath it. For this study, the flux layer thickness is

assumed constant at a typical depth of 10mm. The top of the liquid layer is approximated as a flat surface at the flux melting temperature. The lower surface is set to the molten steel temperature (1550 ^{o}C). The right side of the domain is a symmetry plane, so is an adiabatic, free-slip wall. The left side is in contact with the mold, which should be a wall at the flux solidification temperature. However, to avoid singularity at the left-bottom corner, and to represent the effects of flux leaking into the gap between the steel shell and the mold, the bottom half of the left wall is given a linear temperature profile.

The temperature dependency of the molten flux viscosity is represented by the empirical equation given by [69] as well as curve fits of measurements by [70] and [71].

$$\mu = \mu_0 \frac{T}{T_0} e^{B\left(\frac{1}{T}-\frac{1}{T_0}\right)} \qquad [14]$$

where T_0 is a reference temperature (1773 K), μ0 is a reference viscosity (0.05 Pa·s), and B is a parameter representing the degree of temperature dependency of the flux viscosity.

$$\mu = \mu_0 \left(\frac{T_0 - T_s}{T - T_s}\right)^n \qquad [15]$$

where μ_0 is the viscosity at the reference temperature, T_0 of 1300 ºC, and Ts is the fitting parameter.

The shear velocity along the bottom steel flux interface is varied parametrically to investigate the effect on convection in the liquid flux layer. To match the interfacial shear stress, the liquid flux velocity is much smaller, owing to its higher viscosity. The relationship between flux velocity and steel velocity can be calculated by balancing the interfacial shear stress according to previous work.[72, 73] In this work, constant bottom shear velocities from 0 to 200 mm·s-1 are assumed.

The simulation results show that the Ra number for realistic liquid slag layers varies near the critical Ra number for the onset of natural convection. For fluxes with temperature-dependent viscosity, the variation of Nu with Ra is analogous to correlations for fluids with constant viscosity evaluated at the mean temperature, but the critical Ra number is larger, as shown in **Fig. 12**. The increase in Nu number with layer thickness is also quantified for realistic fluxes. For thin layers of realistic fluxes, natural convection is suppressed, so Nu increases linearly with increase of bottom shear velocity (**Fig. 13**). The increase is greater with decreasing average viscosity. The Nu increases nonlinearly with the increase of steel velocity due to the nonlinear relationship between steel velocity and flux bottom shear

velocity (**Fig. 14**). The increase of heat transfer above pure conduction is only due to end effects, and hence depends on the dimensions of the layer. Larger increases observed in practice could be due to phenomena not included in these computations.

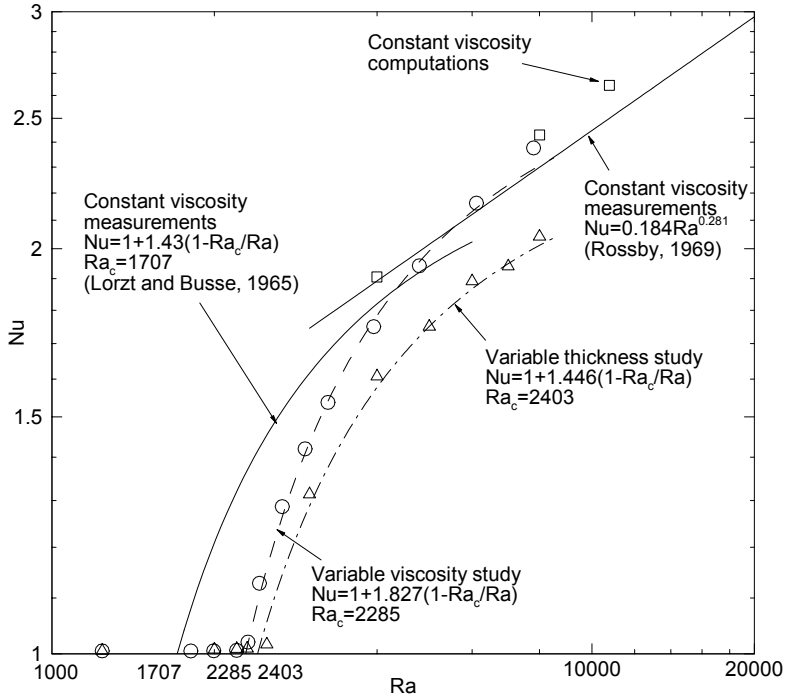

Fig. 12 Heat flow increase with convection strength (symbols are computed and lines are curve fits)

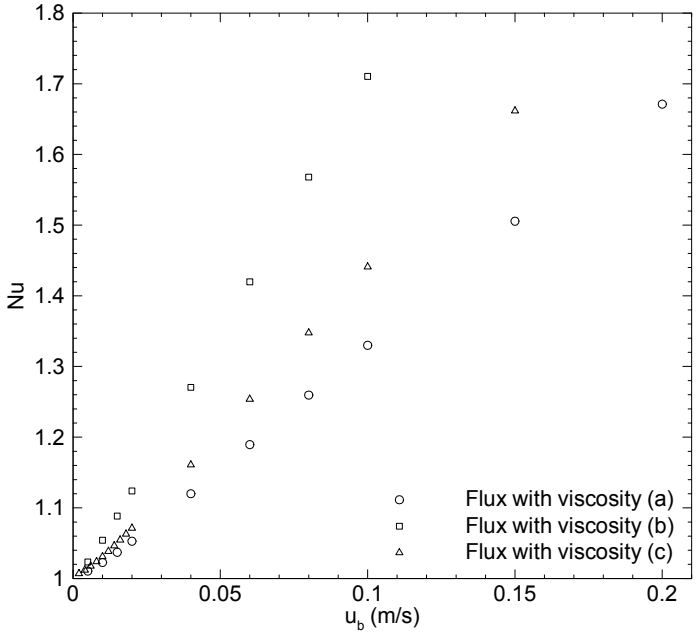

Fig. 13 Nu number as a function of bottom shear velocity

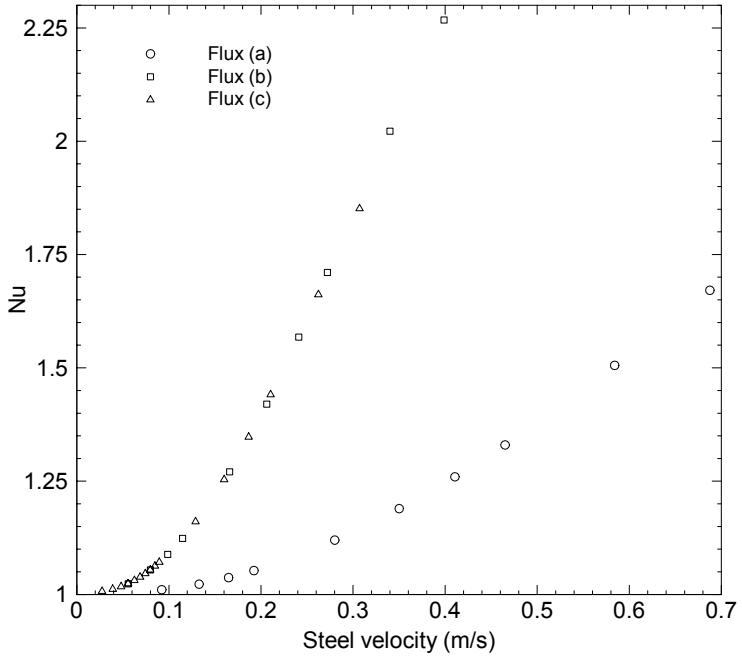

Fig. 14 Nu number as a function of steel velocity

5.5 Transient Flow and Super-Heat Transport in Continuous-Cast Steel Slabs

The flow in the liquid pool region features a steel jet coming out of the submerged nozzle entry and impinging obliquely on the narrow face in a confined space formed by the solidifying steel shell. The jet impingement causes locally high heat transfer rate to the shell. Quantifying the turbulent heat transfer to the shell during the critical early stages of solidification is of great importance to the understanding of phenomena in the casting process, meniscus hook formation, breakouts, internal structure of solidified steel, crack formation, etc. However, the high temperature environment of the process makes it very difficult for experimentation or direct measurement of the flow and temperature field. Scaled or full dimension water models can give some insight into the transient flow features of the process, but with its limitation, water models are unable to generate heat transfer results. Thus, the modeling of transient flow and heat transfer heavily relies on numerical methods. In this work, a large eddy simulation of mold region of a continuous steel caster was carried out to study the turbulent flow and heat transfer.

The simulation domain is one half of a real continuous caster mold region with a section of nozzle. The center plane of narrow face to narrow face is therefore prescribed a symmetry boundary condition which sets normal velocity component and gradients of other variables to zero. The wide faces and the

narrow face are actually solidifying shells of steel and assumed to be straight walls. No-slip boundary conditions are prescribed at the narrow face and the two wide faces. For a caster, the shells are dragged down with the velocity equals to casting speed, so a drag velocity is applied. A constant temperature equals to the solidification temperature of steel was prescribed at the wide and narrow faces as thermal boundary conditions. The outlet of the domain is an artificially cut off plane at 1.2 m below the meniscus, a constant pressure is prescribed at this boundary. It is also assumed that the heat leaving the domain from the outlet is only through convection. The top surface was modeled as a rigid boundary. Free slip boundary condition is prescribed at the top surface. Because of the thermal insulation by the flux, an adiabatic thermal boundary condition is prescribed for the top surface. The inlet condition used for the nozzle is a uniform flow with velocity corresponding to the flow rate. The temperature of the inlet is set to a constant value equals the casting temperature. The length of the nozzle is long enough for the flow to become turbulent when going into the mold. Also the nozzle is modeled as adiabatic as it is made of ceramic material and has good insulation. IX lists the parameters and material properties used in the simulation.

A finite volume code was used to solve the unsteady Navier-Stokes equations. Central differencing with second order accuracy was used to discretize the equations on a collocated grid with variables defined at the cell centers. The time integration of the equations was done using a semi-implicit, fractional step method with diffusion terms treated implicitly by the Crank-Nicolson method. The convective and source terms from SGS stresses are advanced explicitly using the second-order Adams-Bashforth method.

A computational grid consisting of 1.64 million cells was used. The curved surfaces are modeled using a stair step grid. The grid was stretched in the all directions to give finer grid near the solidifying shell.

Average temperature field in the center plane is shown in **Fig. 15**. The jets have very hot cores at the pouring temperature, which diffuses quickly. Most of the jet is roughly 30K above the solidification temperature. Temperature in the upper roll region is quite uniform and has a superheat of about 20K. In the little recirculation at the top right corner, fluid is much cooler: only 5K over the freezing temperature. This is important to meniscus solidification. The coldest regions are near the solidifying shell and the between the wall jet and the center jet low in the domain, where the steel is cooled from both wide faces and there is no strong flow to carry in hotter steel. The important cold region at the

meniscus at the corner of the top surface and the narrow face is caused by the little recirculation region at the corner. This recirculation region is thus detrimental and may cause serious quality problems due to hook formation and inclusion entrapment.[61]

The temperature profiles predicted in the upper roll region are compared with plant measurements in the same caster with the same casting condition. **Figure 16** shows an example comparison of simulation results with the measurements. The temperature profile in the simulations match the experiment very well. This suggests that the temperature field and corresponding heat flux predictions are also accurate.

Figure 17 shows the average heat flux to the solidifying shell along the narrow face. The heat flux is the largest where the jet impinges on the narrow face. There is also a significant time variation, owing to chaotic fluctuations in the jet position. Elsewhere, there is a local heat flux maximum in the wide faces near the narrow face caused by the vortices generated by the impinging of the side jet. There are large regions of relatively high heat flux regions where the side jet, center jet and the wall jets touch the wide faces. In the narrow face, there is a little heat flux rise near the top surface, which is the result of the little recirculation region at the corner. The flow towards the SEN near the top surface creates relatively high heat flux region in the wide faces near the top surface. Also, the vortices generated as the flow towards SEN passes the SEN raise the heat flux to the wide faces above the center jet.

Table IX Parameters and material properties for the simulation

Bottom Nozzle port diameter	32	mm
Domain length (mold part)	1.2	m
Total domain length	1.76	m
Domain thickness	132	mm
Domain width	492	mm
SEN submerge depth	127	mm
Nozzle inlet diameter	70	mm
Side Nozzle port height	75	mm
Side Nozzle port width	32	mm
Casting speed	24.5	$mm \cdot s^{-1}$
Casting temperature	1832	K

Solidus temperature	1775	K
Laminar viscosity	0.00555	$kg \cdot m^{-1} \cdot s^{-1}$
Thermal conductivity	26	$w \cdot m^{-1} \cdot K^{-1}$
Liquid dsteel density	7020	$kg \cdot m^{-3}$
Specific heat of liquid steel	680	$J \cdot kg^{-1} \cdot K^{-1}$
Thermal expansion coefficient	1.0×10-4	K^{-1}
Gravity constant	9.8	$m \cdot s^{-2}$
Laminar prandtl number	0.1452	
Turbulent prandtl number	0.9	

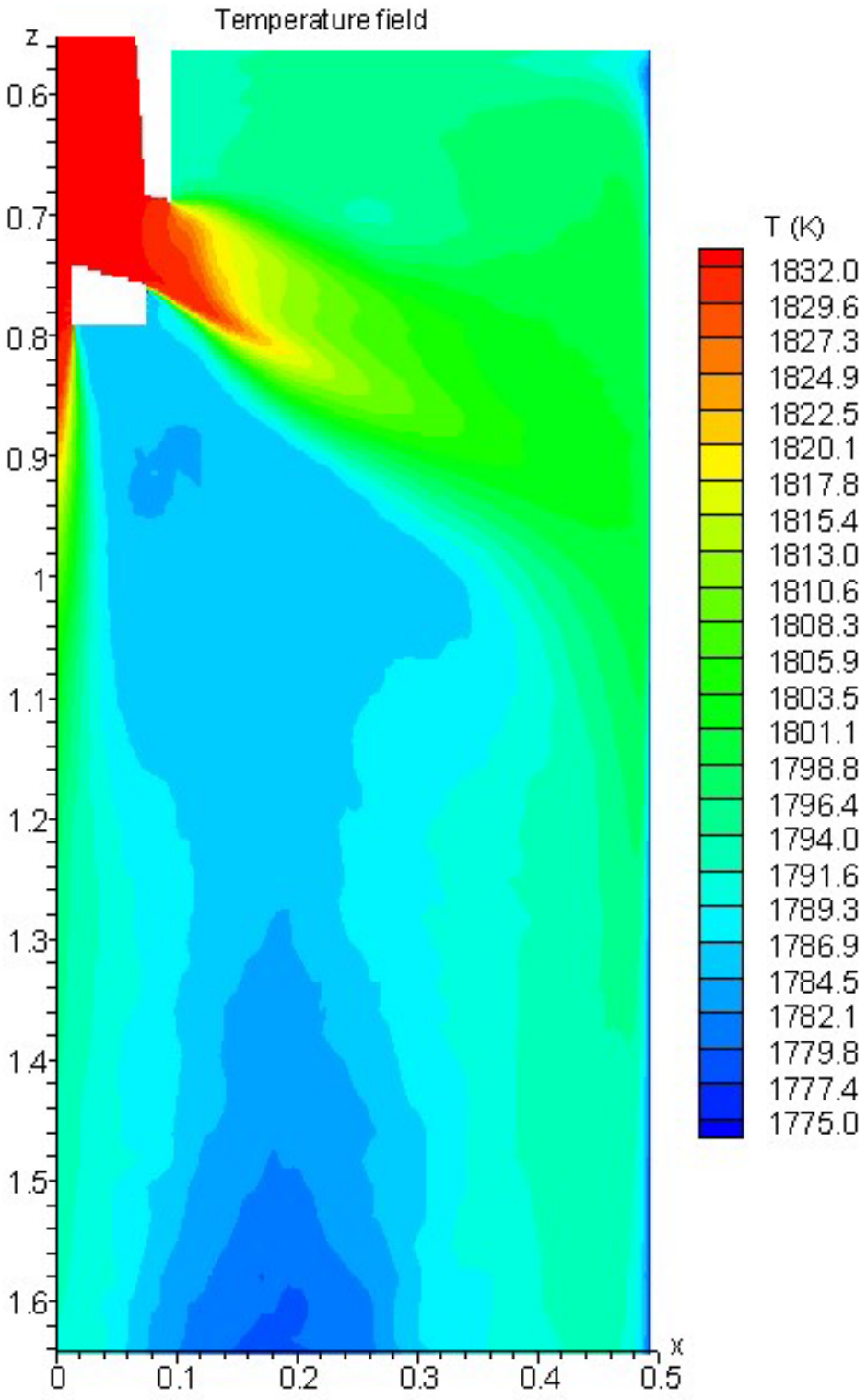

Fig. 15 Mean temperature field of center plane (with SGS model)

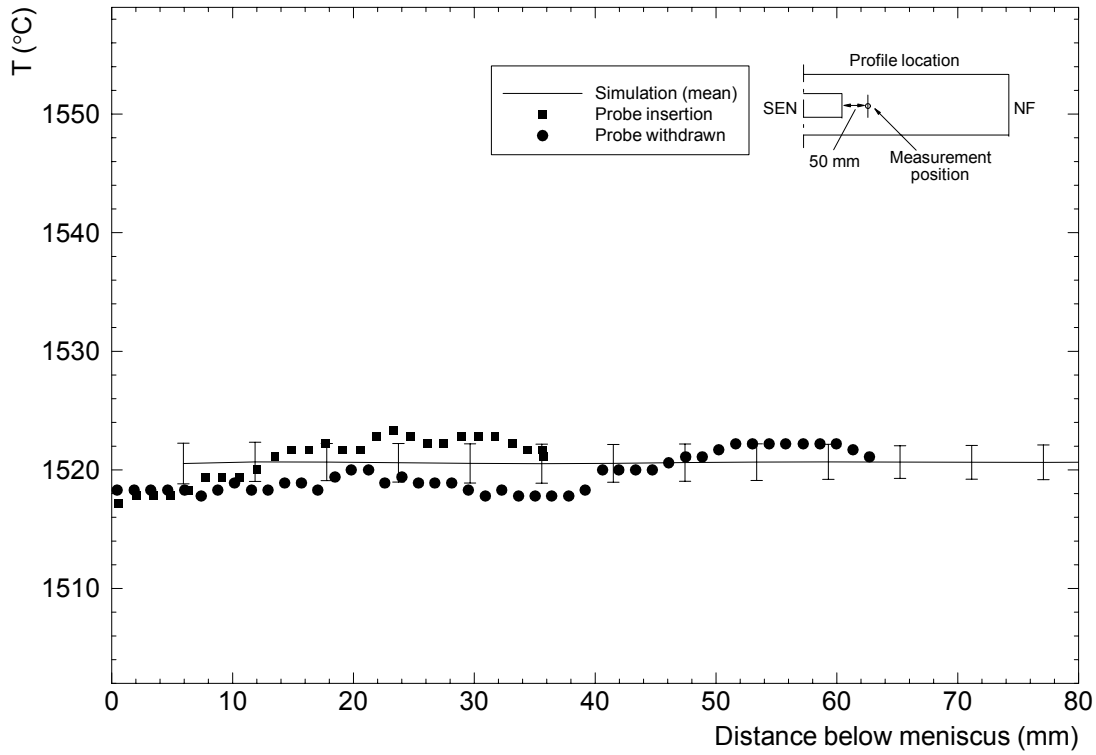

Fig. 16 Simulated and measured temperature profiles in molten steel (measurement 1, with SGS model)

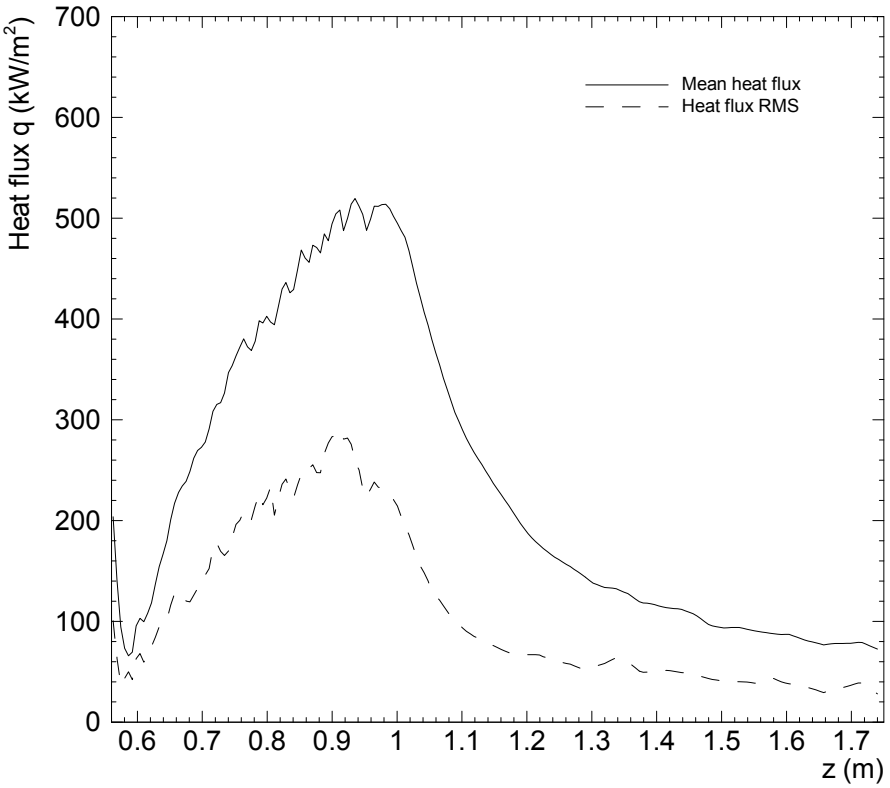

Fig. 17 Heat fluxes profile along narrow face centerline (with SGS model)

6. SIGNIFICANT FINDINGS

Advanced computational models are being developed to predict quantitatively, the removal of inclusions in the mold region during the continuous casting steel. This multi-faceted research project includes models of transient fluid flow in the nozzle and mold, fluctuation of the top free surface, and the transport of heat and inclusion particles. The final system of models will incorporate the results of other models, including: 1) nucleation and growth to find the inclusion size distributions, 2) argon bubble size distribution, relative rising velocity, and inclusion attachment probability, and 3) entrapment criteria at the solidification front and top surface. Each aspect of the models is being tested through extensive comparison with measurements, including the measurement of total inclusion entrapment in the cast steel product at the plant. Work this past year has obtained several new findings, which are significant to the accurate prediction of inclusion behavior in continuous casting.

1) At least 2500 particles are required to obtain statistics accurate within ±3% for inclusion transport in the mold. The initial removal rates are chaotic, and depend on time variations in the flow.

2) Inclusion particle entrapment locations in the final product are predicted and compared with measurements: only a small fraction of the total inclusions entering the caster (which are mainly smaller than 30μm) appear to be removed, so there is great incentive to remove them during upstream processing. The removal of larger inclusions is more difficult both to measure and to compute, but is the focus of continuing efforts, owing to its greater importance to steel quality.

3) A short (9s) burst of inclusions entering the caster takes about 4 minutes to remove for the casting conditions assumed here. The captured particles concentrate mainly within a 2-m long section of slab. Using this information from together with sensors to detect when inclusion bursts occur would allow the contaminated steel to be isolated.

4) Flow transport tends to concentrate entrapped inclusions within 10-20mm beneath the strand surface, especially at the corner and towards the narrow faces. Thus, it is appropriate to focus inspection and slab conditioning efforts on improving the surface.

5) Particle entrapment on refractory walls is a significant inclusion removal mechanism in addition to being associated with nozzle clogging, sudden release, and other quality problems.

6) An efficient size-grouping model has been developed to simulate collisions in order to better model inclusion size distribution evolution starting from nucleation to final product size.

7) Mixing computations have been developed to establish an accurate methodology for future inclusion particle motion, in addition to investigating inclusion removal during upstream processes.

8) Correlations have been developed to predict surface heat removal through the flux layer as a function of its thickness, properties, and the fluid velocity beneath it. Natural convection is significant only at the corners of the layer. These results will be useful in further models of the crucial meniscus region, which governs inclusion entrapment at the meniscus and other surface quality problems.

9) Methodologies to accurately predict superheat transport during flowing molten metal have been developed, validated with plant measurements and applied to real casters. This benchmark computation will be important for further model validation and parametric studies to lessen problems with excessive shell thinning at the impingement point, and excessive meniscus solidification (and the corresponding inclusion entrapment).

7. IMPACT

This work aims to improve understanding of the transient flow of molten steel, superheat, and inclusions during the continuous casting of steel slabs, through the development, validation, and application of fundamental computational models of transient fluid flow and heat transfer. It further aims to predict quantitatively how inclusions are entrapped and to evaluate methods to lower inclusion-related defects. Plant observations have found that many serious quality problems, including inclusion entrapment, are directly associated with the flow pattern in the mold. The results from the computational simulations of this work are increasing fundamental understanding of transient fluid flow, gas, and inclusion particle transport in the mold region. This will lead to optimized nozzle geometry and gas flow rates to improve mold flow patterns and minimize inclusion defects. Lowering defects from internal inclusions can improve steel minimum strength, fatigue life, surface appearance, yield and energy efficiency (from reduced rejects) and lower production cost. Furthermore, the computational tools developed and validated in this work can be applied to study and optimize flow in other processes.

8. ACKNOWLEDGMENTS

The authors wish to thank the National Science Foundation (Grant # DMI-01-15486) and the Continuous Casting Consortium (Accumold, Huron Park, Ontario; AK Steel, Middletown, OH; Swedish Institute for Metals Research, Stockholm, Sweden; and Postech, Pohang, S. Korea) is gratefully acknowledged. Thanks are also extended to industry researchers Ron O'Malley, formerly at AK Steel,

P. Dauby, formerly at LTV Steel, and others who helped to obtain samples and plant data. Finally, thanks are due to FLUENT, Inc., for providing the FLUENT code, and to the National Center for Supercomputing Applications at the University of Illinois for computing time.

9. REFERENCES

1. "Continuously Cast Steel Output, 1999," Report, International Iron Steel Institute, Brussels, Belgium, 2000, www.worldsteel.org.
2. J. Herbertson, Q.L. He, P.J. Flint, R.B. Mahapatra, "Modelling of Metal Delivery to Continuous Casting Moulds," in Steelmaking Conf. Proc., Vol. 74, ISS, Warrendale, PA, (Washington, D.C.), 1991, 171-185.
3. T. Honeyands and J. Herbertson, "Oscillations in Thin Slab Caster Mold Flows," 127th ISIJ Meeting, ISIJ, Tokyo, Japan, 1994.
4. B.G. Thomas, "Application of Mathematical Models to the Contious Slab Casting Mold.," Iron & Steelmaker (ISS Trans.), Vol. 16 (12), 1989, 53-66.
5. B.G. Thomas, "Mathematical Modeling of the Continuous Slab Casting Mold, a State of the Art Review," in Mold Operation for Quality and Productivity, A. Cramb, ed. Iron and Steel Society, Warrendale, PA, 1991, 69-82.
6. B.G. Thomas and F.M. Najjar, "Finite-Element Modeling of Turbulent Fluid Flow and Heat Transfer in Continuous Casting," Applied Mathematical Modeling, Vol. 15 (5), 1991, 226-243.
7. X. Huang, B.G. Thomas and F.M. Najjar, "Modeling Superheat Removal during Continuous Casting of Steel Slabs," Metall. Trans. B, Vol. 23B (6), 1992, 339-356.
8. X. Huang and B.G. Thomas, "Modeling of Steel Grade Transition in Continuous Slab Casting Processes," Metall. Trans., Vol. 24B (2), 1993, 379-393.
9. D.E. Hershey, B.G. Thomas and F.M. Najjar, "Turbulent Flow through Bifurcated Nozzles," Int. J. Num. Meth. in Fluids, Vol. 17 (1), 1993, 23-47.
10. B.G. Thomas and X. Huang, "Effect of Argon Gas on Fluid Flow in a Continuous Slab Casting Mold," in 76th Steelmaking Conf. Proc., Vol. 76, Iron and Steel Society, Warrendale, PA, (Dallas, TX), 1993, 273-289.
11. B.G. Thomas, X. Huang and R.C. Sussman, "Simulation of Argon Gas Flow Effects in a Continuous Slab Caster," Metall. Trans. B, Vol. 25B (4), 1994, 527-547.
12. G.D. Lawson, S.C. Sander, W.H. Emling, A. Moitra, B.G. Thomas, "Prevention of Shell Thinning Breakouts Associated with Widening Width Changes," in Steelmaking Conf. Proc., Vol. 77, ISS, Warrendale, PA, (Chicago, IL), 1994, 329-336.
13. F.M. Najjar, B.G. Thomas and D.E. Hershey, "Turbulent Flow Simulations in Bifurcated Nozzles: Effects of Design and Casting Operation," Metall. Trans. B, Vol. 26B (4), 1995, 749-765.
14. R. McDavid and B.G. Thomas, "Flow and Thermal Behavior of the Top-Surface Flux/ Powder Layers in Continuous Casting Molds," Metall. Trans. B, Vol. 27B (4), 1996, 672-685.
15. B.G. Thomas, A. Denissov and H. Bai, "Behavior of Argon Bubbles during Continuous Casting of Steel," in Steelmaking Conf. Proc., Vol. 80, ISS, Warrendale, PA., (Chicago, IL), 1997, 375-384.
16. B.G. Thomas, R. O'Malley, T. Shi, Y. Meng, D. Creech, D. Stone, "Validation of Fluid Flow and Solidification Simulation of a Continuous Thin Slab Caster," in Modeling of Casting, Welding,

and Advanced Solidification Processes, Vol. IX, Shaker Verlag GmbH, Aachen, Germany, (Aachen, Germany, August 20-25, 2000), 2000, 769-776.
17. H. Bai and B.G. Thomas, "Bubble Formation during Horizontal Gas Injection into Downward Flowing Liquid," Metall. Mater. Trans. B, Vol. 32B (6), 2001, 1143-1159.
18. H. Bai and B.G. Thomas, "Turbulent Flow of Liquid Steel and Argon Bubbles in Slide-Gate Tundish Nozzles, Part I, Model Development and Validation," Metall. Mater. Trans. B, Vol. 32B (2), 2001, 253-267.
19. H. Bai and B.G. Thomas, "Turbulent Flow of Liquid Steel and Argon Bubbles in Slide-Gate Tundish Nozzles, Part II, Effect of Operation Conditions and Nozzle Design," Metall. Mater. Trans. B, Vol. 32B (2), 2001, 269-284.
20. H. Bai and B.G. Thomas, "Effects of Clogging, Argon Injection and Continuous Casting Conditions on Flow and Air Aspiration in Submerged Entry Nozzles," Metall. Mater. Trans. B, Vol. 32B (4), 2001, 707-722.
21. B.G. Thomas and H. Bai, "Tundish Nozzle Clogging – Application of Computational Models," in Steelmaking Conf. Proc., Vol. 18, Iron and Steel Society, Warrendale, PA, (Baltimore, MD), 2001, 895-912.
22. B.G. Thomas, "Modeling Study of Intermixing in Tundish and Strand during a Continuous-Casting Grade Transition," Iron and Steelmaker, Vol. 24 (12), 1997, 83-96.
23. X. Huang and B.G. Thomas, "Modeling of Transient Flow Phenomena in Continuous Casting of Steel," Canadian Metall. Quart., Vol. 37 (304), 1998, 197-212.
24. B.G. Thomas, H. Bai, S. Sivaramakrishnan, S.P. Vanka, "Detailed Simulation of Flow in Continuous Casting of Steel Using K-ε, LES, and PIV," International Symposium on Cutting Edge of Computer Simulation of Solidification and Processes, (Osaka, Japan, Nov. 14-16, 1999), ISIJ, 1999, 113-128.
25. B.G. Thomas and S.P. Vanka, "Study of Transient Flow Structures in the Continuous Casting of Steel," NSF Design & Manufacturing Grantees Conference, (Long Beach, CA), NSF, Washington, D.C., 1999.
26. B.G. Thomas and S.P. Vanka, "Study of Transient Flow Structures in the Continuous Casting of Steel," NSF Design & Manufacturing Grantees Conference, (Vancouver, Canada), NSF, Washington, D.C., 2000, 14p.
27. S.P. Vanka and B.G. Thomas, "Study of Transient Flow Structures in the Continuous Casting of Steel," NSF Design & Manufacturing Grantees Conference, (Jan. 7-10, Tampa, FL), NSF, Washington, D.C., 2001, 14p.
28. S. Sivaramakrishnan, H. Bai, B.G. Thomas, P. Vanka, P. Dauby, M. Assar, "Transient Flow Structures in Continuous Cast Steel," in Ironmaking Conference Proceedings, Vol. 59, ISS, Warrendale, PA, (Pittsburgh, PA, March 26-29, 2000), 2000, 541-557.
29. S. Sivaramakrishnan, B.G. Thomas and S.P. Vanka, "Large Eddy Simulation of Turbulent Flow in Continuous Casting of Steel," in Materials Processing in the Computer Age, Vol. 3, V. Voller and H. Henein, eds., TMS, Warrendale, PA, 2000, 189-198.
30. B.G. Thomas, "Modeling of the Continuous Casting of Steel: Past, Present, and Future, Dr. J. Keith Brimacombe Lecture," in Electric Furnace Conf. Proc., Vol. 59, ISS, Warrendale, PA, (Phoenix, AZ), 2001, 3-30.
31. W.H. Emling, T.A. Waugaman, S.L. Feldbauer, A.W. Cramb, "Subsurface Mold Slag Entrainment in Ultra-Low Carbon Steels," in Steelmaking Conf. Proc., Vol. 77, ISS, Warrendale, PA, (Chicago, IL), 1994, 371-379.

32. R.C. Sussman, M. Burns, X. Huang, B.G. Thomas, "Inclusion Particle Behavior in a Continuous Slab Casting Mold," in 10th Process Technology Conference Proc., Vol. 10, Iron and Steel Society, Warrendale, PA, (Toronto, Canada, April 5-8, 1992), 1992, 291-304.
33. B.G. Thomas, Q. Yuan, L. Zhang, S.P. Vanka, "Flow Dynamics and Inclusion Transport in Continuous Casting of Steel," in 2003 NSF Design, Service, and Manufacturing Grantees and Research Conf. Proceedings, R.G. Reddy, ed. University of Alabama, Tuscaloosa, AL 35498, (Burmingham, AL), 2003, 2328-2362.
34. B.G. Thomas and T. Morthland, "3-D Heat Transfer Analysis of Columbus Slab Casting Mold," Report, Research Report to Columbus Steel, 2001.
35. B.G. Thomas, "Modeling of the Continuous Casting of Steel: Past, Present, and Future, Dr. J. Keith Brimacombe Lecture," Metal. & Material Trans., Vol. 33B (Dec.), 2002, 795-812.
36. B.G. Thomas, Q. Yuan, L. Zhang, S.P. Vanka, "Flow Dynamics and Inclusion Transport in Continuous Casting of Steel," in 2002 NSF Design, Service, Manufacturing and Industrial Innovation Research Conf. Proceedings, National Science Foundation, Washington, D.C., (San Juan, Puerto Rico), 2002, 22p.
37. L. Zhang, W. Pluschkell, and B.G. Thomas, "Nucleation and Growth of Alumina Inclusions During Steel Deoxidation," in Steelmaking Conf. Proc., Vol. 85, ISS, Warrendale, PA, (Nashville, March 10-13, 2002), 2002, 463-476.
38. L. Zhang, B.G. Thomas, X. Wang, and K. Cai, "Evaluation And Control Of Steel Cleanliness - A Review," in Steelmaking Conf. Proc., Vol. 85, ISS, Warrendale, PA, (Nashville, TN, March 10-13, 2002), 2002, 431-452.
39. L. Zhang and B.G. Thomas, "Alumina Inclusion Behavior During Steel Deoxidation," 7th European Electric Steelmaking Conference, (May 26-29, 2002, Venice, Italy), Associazione Italiana di Metallurgia, Milano, Italy, Vol. 2, 2002, 2.77-2.86.
40. B.G. Thomas, "Annual Report to Continuous Casting Consortium," Report, University of Illinois at Urbana-Champaign, 2002.
41. L. Zhang and B.G. Thomas, "State of the Art in Evaluation and Control of Steel Cleanliness," ISIJ International, Vol. 43 (3), 2003, 271-291.
42. Y. Meng and B.G. Thomas, "Heat Transfer and Solidification Model of Continuous Slab Casting: CON1D," Metal. & Material Trans., Vol. 34B (5), 2003, 685-705.
43. Y. Meng and B.G. Thomas, "Interfacial Friction-Related Phenomena in Continuous Casting with Mold Slags," in ISSTech 2003 Steelmaking Conf. Proc., Vol. 86, ISS, Warrendale, PA, (Indianapolis, IN, Apr. 27-30, 2003), 2003, 589-606.
44. Y. Meng and B.G. Thomas, "Interfacial Friction-Related Phenomena in Continuous Casting with Mold Slags," Metall. & Materials Trans. B, Vol. 34B (5), 2003, 707-725.
45. Q. Yuan, B.G. Thomas and S.P. Vanka, "Turbulent Flow and Particle Motion in Continuous Slab-Casting Molds," in ISSTech 2003 Process Technology Proceedings, Vol. 86, ISS, Warrendale, PA, (Indianapolis, IN, Apr 27-30, 2003), 2003, 913-927.
46. L. Zhang, B.G. Thomas, Kaike Cai, Jian Cui, L. Zhu, "Inclusion Investigation during Clean Steel Production at Baosteel," in ISSTech 2003 Steelmaking Conf. Proc., Vol. 86, ISS, Warrendale, PA, (Indianapolis, IN, Apr. 27-30, 2003), 2003, 141-156.
47. Q. Yuan, S.P. Vanka and B.G. Thomas, "Large Eddy Simulations of Transient Flow during Continuous Slab Casting of Steel," in 3rd International Symposium on Turbulenece and Shear Flow Phenomena, Vol. 2, (Sendai, Japan, June 25-27, 2003), 2003, 681-686.

48. B.G. Thomas, "On-line Detection of Quality Problems in Continuous Casting of Steel," in Proceedings of the International Symposium on Process Control and Optimization in Ferrous and Nonferrous Industry, TMS, Warrendale, PA, (Chicago, IL, Nov. 10-12, 2003), 2003.
49. L. Zhang and B.G. Thomas, "Inclusions in Continuous Casting of Steel", XXIV National Steelmaking Symposium,," in XXIV National Steelmaking Symposium, (Morelia, Mich, Mexico, Nov. 26-28, 2003), 2003, 42p.
50. L. Zhang and B.G. Thomas, "Fluid Flow and Inclusion Motion in the Continuous Casting Strand," in XXIV National Steelmaking Symposium, (Morelia, Mich, Mexico, Nov. 26-28, 2003), 2003, 13p.
51. L. Zhang and B.G. Thomas, "Inclusion Nucleation, Growth, and Mixing during Steel Deoxidation," Report No. CCC200206, University of Illinois at Urbana-Champaign, 2003.
52. M. Jenkins, B.G. Thomas and R.B. Mahapatra, "Investigation of Strand Surface Defects Using Mold Instrumentation and Modeling," Ironmaking and Steelmaking, 2003, submitted August, 2003.
53. Q. Yuan, B.G. Thomas and S.P. Vanka, "Study of Transient Flow and Particle Transport during Continuous Casting of Steel Slabs, Part 1. Fluid Flow," Metall. & Materials Trans. B, submitted August, 2003.
54. Q. Yuan, B.G. Thomas and S.P. Vanka, "Study of Transient Flow and Particle Transport during Continuous Casting of Steel Slabs, Part 2. Particle Transport," Metall. & Materials Trans. B, accepted October, 2003.
55. B. Zhao, S.P. Vanka and B.G. Thomas, "Numerical Study of Flow and Heat Transfer in a Molten Flux Layer," Int. J. Heat and Fluid Flow, submitted September, 2003.
56. B.G. Thomas, "Continuous Casting," in Yearbook of Science and Technology, McGraw-Hill, 2004, in press.
57. Q. Yuan, "Modeling of Particle Engulfment / Pushing at Solidification Front during Continuous Casting of Steel," Report, University of Illinois at Urbana-Champaign, 2002.
58. B.G. Thomas, R.J. O'Malley and D.T. Stone, "Measurement of temperature, solidification, and microstructure in a continuous cast thin slab," Modeling of Casting, Welding, and Advanced Solidification Processes, (San Diego, CA), TMS, Warrendale, PA, Vol. VIII, 1998, 1185-1199.
59. W.H. Press, B.P. Flannery, S.A. Teukolsky, W.T. Vetterling, Numerical Recipes, Cambridge University Press, New York, NY, 1988, 963.
60. Y. Miki and B.G. Thomas, "Modeling of Inclusion Removal in a Tundish," Metall. Mater. Trans. B, Vol. 30B (4), 1999, 639-654.
61. B.G. Thomas, "Chapter 14. Fluid Flow in the Mold," in Making, Shaping and Treating of Steel: Continuous Casting, Vol. 5, A. Cramb, ed. AISE Steel Foundation, Pittsburgh, PA, 2003, 14.1-14.41.
62. J.H. Schade, R.J. O'Malley, F.L. Kemeny, Y. Sahai, D.J. Zacharias, "Chapter 13: Tundish Operations," in The Making, Shaping and Treating of Steel, 11th Edition, Casting Volume, A.W. Cramb, ed. The AISE Steel Foundation, (Pittsburgh, PA), 2003, 70.
63. J. Knoepke, M. Hubbard, J. Kelly, R. Kittridge, J. Lucas, "Pencil Blister Reduction at Inland Steel Company," in Steelmaking Conf. Proc., Vol. 77, ISS, Warrendale, PA, (Chicago, IL), 1994, 381-388.
64. B. Grimm, P. Andrzejewski, K. Muller, K.-H. Tacke, "Inclusions in Continuously Cast Steel Slabs-Numerical Model and Validation," Steel Res., Vol. 70 (10), 1999,
65. O. Nomura, "Influence of Continuous Casting Submerged Nozzle on Quality of Cast Steel," Seramikkusu (Ceramics Japan), Vol. 35 (8), 2000, 617-621.

66. FLUENT5.1, Report, Fluent Inc., Lebanon, New Hampshire, 2000.
67. P.G.Saffman and J.S.Turner, J. Fluid Mechanics, Vol. 1, 1956, 16-30.
68. J. Szekely, C.W. Chang and T. Lehner, "Flow Phenomena, Mixing and Mass Transfer in Argon-Stirred Ladles," Ironmaking & Steelmakaing, Vol. 6, 1979, 285.
69. P.V. Riboud and M. Larrecq, "Steelmaking Proceedings," ISS-AIME, Vol. 62 (1979), 1979, 78-92.
70. D. Larson, "Criteria for Selecting Mold Powders to Optimize Continuous Cast Steel Quality," Industrial Heating, Vol. 53, 1986, 16-19.
71. M.D. Lanyi and C.J. Rosa, "Viscosity of Casting Fluxes Used During Continuous Casting of Steel," Metallurgical and Materials Transactions B, Vol. 12B, 1981, 287-298.
72. R.M. McDavid and B.G. Thomas, "Flow and Thermal Behavior of the Top Surface Flux/Powder Layers in Continuous Casting Molds," Metallurgical and Materials Transactions B, Vol. 27B, 1996, 672-685.
73. S. Sivaramakrishnan, "Large Eddy Simulation, Particle Image Velocimetry in the Study of Mold Transients in Continuous Casting of Steel and Heat Transfer through Molten Slag Layers," M.S. Thesis, University of Illinois at Urbana-Champaign, 2000,